

Contents lists available at ScienceDirect

Journal of Computational Physics: X

journal homepage: www.elsevier.com/locate/jcpx



Discontinuous Galerkin spectral element method for shock capturing with summation by parts properties



Fengrui Zhang*, Yulia T. Peet

School for Engineering of Matter, Transport and Energy, Arizona State University, Tempe, AZ, 85287, USA

ARTICLE INFO

Article history: Received 31 August 2020 Received in revised form 21 February 2022 Accepted 1 January 2023 Available online 6 January 2023

Keywords:
Discontinuous Galerkin spectral element
method
Summation by parts
Shock capturing
High order
Entropy viscosity
Split form

ABSTRACT

This paper presents a computational methodology developed for a high-order approximation of compressible fluid dynamics equations with discontinuities. The methodology is based on a discontinuous Galerkin spectral-element method (DGSEM) built upon a split discretization framework with summation-by-parts (SBP) property, which mimics the integration-by-parts operation in a discrete sense. To extend the split DGSEM framework to discontinuous cases, we implement a shock capturing method based on the entropy viscosity formulation. The developed high-order split-form DGSEM with shock-capturing methodology is subject to a series of evaluation on both one-dimensional and twodimensional, continuous and discontinuous cases. Convergence of the method is demonstrated both for smooth and shocked cases that have analytical solutions. The 2D Riemann problem tests illustrate an accurate representation of all the relevant flow phenomena, such as shocks, contact discontinuities, and rarefaction waves. All test cases are able to run with a polynomial order of 7 or higher. The values of the tunable parameters related to the entropy viscosity are robust for both 1D and 2D test problems. We also show that higherorder approximations yield smaller errors than lower-order approximations, for the same number of total degrees of freedom.

© 2023 Published by Elsevier Inc. This is an open access article under the CC BY-NC-ND license (http://creativecommons.org/licenses/by-nc-nd/4.0/).

1. Introduction

The pursuit of high-order numerical schemes is necessary, especially when an efficient resolution of the multiscale solution features is required. Numerical investigation [1] shows that with the same number of degrees of freedom, increasing the polynomial order gives a higher accuracy result. In previous works using a discontinuous Galerkin finite element method (DGFEM), the polynomial order is typically no higher than 5 [2–6], while those applying a spectral element method (DGSEM) have higher polynomial orders [1,7,8]. This is partly owing to diagonal mass matrix properties of the DGSEM arising from its nodal basis approximation [9], which makes its implementation more efficient and thus attainable with high polynomial orders.

The goal of this work is to build up a framework that enjoys high polynomial orders in problems with discontinuities. There are two major ingredients that are implemented in this paper: 1) a split-form DGSEM with SBP property, 2) a shock-capturing principle based on the gridpoint-wise artificial viscosity formulation. In what follows, we present the motivation behind these two approaches.

E-mail addresses: fzhang82@asu.edu (F. Zhang), ypeet@asu.edu (Y.T. Peet).

^{*} Corresponding author.

The SBP operator, commonly combined with the simultaneous approximation terms (SAT) for the interfaces and boundaries, has been widely employed in the finite difference community due to its superior stability property from an energy estimate perspective [10–13]. The relationship between the SBP-SAT framework and DGSEM with Gauss-Legendre-Lobatto (GLL) points is discussed in [14–16,7,17] demonstrating that DGSEM-GLL can be considered as an SBP-SAT operator with a diagonal norm. The SBP operation is a mimic of the integration-by-parts process in a discrete sense. The DGSEM-GLL with SBP property can be derived from the weak form DGSEM by applying integration-by-parts once again to the volume contribution. We should note that the new form is also the strong form DGSEM, and because of the SBP property, the weak form DGSEM is algebraically equivalent to the strong form DGSEM. An SBP framework on a more general node set is presented in [18]. One may not be restricted to the GLL points, instead, it is shown that the choice of quadrature points can be flexible, e.g., Gauss-Legendre (GL) points [19]. In the current paper, we retain the formulation on GLL points since it doesn't require extra interpolation routines and an additional storage for the flux points on the element boundaries. The comparison of GLL and GL quadrature rules in DGSEM can be found in [20].

Due to a reduced amount of numerical dissipation in high-order approximations, the aliasing error occurring in a numerical discretization of non-linear terms can contaminate the solution and cause instabilities. The most common ways of controlling the aliasing error in high-order finite/spectral element methods are: 1) de-aliasing, or over-integration, 2) polynomial filtering. The first technique, over-integration, is directly geared towards eliminating the aliasing error arising from the insufficient quadrature of the nonlinear terms by increasing the number of quadrature points up to 3/2 times of the original number [21–23]. While in incompressible flows this technique does lead to a recovery of an exact integration rule for nonlinear terms due to a quadratic nature of non-linearity [21,23], it does not do so in compressible flows, where nonlinearity is rational [24]. Another drawback of the over-integration technique is that by increasing the number of integration points it also increases the computational cost. With polynomial filtering, an energy piled up in a high-frequency part of the spectrum due to aliasing is removed by application of a high-pass filter [25,26,1]. A drawback of the filtering technique is its essentially dissipative nature, and a lack of a clear connection between the adjustable parameters, such as the cut-off wave number and the filtering weights, and an amount of the added dissipation, which makes it hard to precisely adjust or control.

In the finite difference community, an alternative method to reduce the non-linearity-induced aliasing error is to rewrite the non-linear convection terms into a split form. Mathematically, there are various ways to reformulate the non-linear product, leading to a family of split forms [27–30]. With a careful choice of the splitting method, it allows for the conservation of a secondary quantity, e.g., kinetic energy or entropy. Since the split-form operator alone is not conservative, it is commonly used within the previously mentioned SBP framework. It is proven that with a diagonal norm SBP operator, any split form can be rewritten into a telescoping flux differencing form, which allows one to apply the Lax-Wendroff theorem to show that the solution satisfies the governing equations weakly if convergent [31]. Thus in this framework, the split form may enjoy the conservation of a secondary quantity and the primary quantities (conserved variables) simultaneously. Such appealing properties are also introduced into the DG community. As mentioned previously, DGSEM-GLL with SBP property is also a diagonal norm SBP operator. Authors in [7] further show that the split form of the volume contribution is equivalent to the corresponding numerical volume flux. In the present paper, we restrict our choice to the Pirozzoli flux to build up a framework with kinetic-energy-preserving property.

While the split-form DGSEM schemes in the SBP framework have by now been studied quite extensively in the context of continuous problems, the goal of the current paper is to extend the split-form DGSEM formulation to discontinuous cases. In the presence of discontinuities, another type of instability arises, in addition to the aliasing instability, namely, Gibbs instability, which needs to be dealt with, using the approaches commonly known as shock-capturing methods. In [32-34], an extension of a split-form DGSEM to shocked cases is presented using a subcell finite volume method (FVM) shockcapturing scheme. In this technique, a modal-based indicator is employed to switch between DGSEM in smooth areas and FVM in shocked areas. This is essentially done by blending the FV flux with the DG flux, utilizing a blending coefficient (if only FV flux is applied [32], the blending coefficient equals to 1), which is computed element-wise. To take advantage of the high-order accuracy of DGSEM, it is desirable, however, to activate the shock capturing scheme only on "troubled" GLL points rather than the whole element. In order to accomplish this, we turn our attention to shock-capturing schemes which would allow for such a localized treatment of shock boundaries. Among the methods that can potentially accomplish this are: 1) limiting techniques [2,35,36,4]; 2) artificial viscosity methods [3,37,5,38-42]. Among the literature employing the limiting techniques, [4] requires least inter-element communication but still needs a substantial amount of information from the neighbor elements for reconstruction. In the artificial viscosity method, the stabilization is achieved by adding artificial diffusion terms that take the form of the Laplacian of the conserved variables multiplied by a gridpoint-wise value of the viscosity coefficient, thus assuring both compactness and a sub-element resolution of discontinuities. The diffusive coefficient is calculated using shock detectors [3,37]. In the presented methodology, the entropy-residual based shock detector [37,42] is employed, which is directly related to the entropy production caused by discontinuities. To activate the artificial viscosity only in the shocked regions and avoid an excessive dissipation of the solution in the smooth areas, we augment the entropy-based shock detector with the modified Ducros sensor [29,43]. We note that the developed viscous regularization technique, apart from being an effective shock-capturing scheme, can also be effective for stabilization of continuous but severely under-resolved problems, such as an inviscid Kelvin-Helmholtz instability case considered here. The current paper can be considered as a contribution towards development, benchmarking and verification of split-form DGSEM-SBP methods with shock-capturing properties.

The developed methodology based on a split-form discontinuous Galerkin spectral element method with SBP operators and viscous shock capturing is built within the open-source spectral-element code Nek5000 [44]. The methodology is shown to be robust for a variety of continuous and discontinuous compressible flow problems, including problems with strong shocks. We note that one of the drawbacks of viscous shock capturing is related to a stringent stability bound on a time step with explicit time integration schemes when the added viscosity values are large.

The paper is organized as follows. Section 2 is devoted to the description of the numerical methodology, and documents, in turn, a standard DGSEM approach, split-form DGSEM with the SBP operators, and split DGSEM-SBP with the viscous regularization artificial viscosity method for shock capturing. Section 3 presents the results of verification and benchmarking of the developed numerical methodology on the example of test problems, including two smooth problems and six shocked problems, in 1D and 2D settings. Convergence of the algorithm is also demonstrated with and without the presence of discontinuities. In all the cases, the simulations are stable with a polynomial order of at least as high as 7. The main content is concluded in Section 4.

2. Numerical methodology

The governing equations in the current study are the Euler equations

$$\frac{\partial \mathbf{U}}{\partial t} + \nabla \cdot \mathbf{F} = 0, \tag{1}$$

$$\mathbf{U} = \begin{pmatrix} \rho \\ \rho \mathbf{u} \\ \rho e \end{pmatrix}, \mathbf{F} = \begin{pmatrix} \rho \mathbf{u}^T \\ \rho \mathbf{u} \otimes \mathbf{u} + \mathbf{I} p \\ \rho e \mathbf{u}^T + p \mathbf{u}^T \end{pmatrix}, \tag{2}$$

where ρ is the density, $\mathbf{u} = (u_1, u_2)^T$ is the velocity vector, e is the total energy per unit mass, p is the pressure, \mathbf{I} is the identity matrix, \otimes denotes the tensor product operator, and the superscript "T" denotes a matrix transpose. To close the system, the ideal gas equation of state, and the relation between the temperature and the total energy per unit mass are introduced.

$$p = \rho RT, \tag{3}$$

$$e_{internal} = C_{\nu} T = e - \frac{1}{2} |\mathbf{u}|^2. \tag{4}$$

2.1. Standard DGSEM

In two dimensions, (1) can be written as

$$\frac{\partial \mathbf{U}}{\partial t} + \frac{\partial \mathbf{F}_1}{\partial x} + \frac{\partial \mathbf{F}_2}{\partial y} = 0,\tag{5}$$

where \mathbf{F}_1 and \mathbf{F}_2 are the corresponding columns of the matrix \mathbf{F} . The domain is decomposed into non-overlapping quadrilateral elements. Each element is transformed from a physical domain $\mathbf{x} = (x, y) = (x_1, x_2)$ into a computational reference domain $\boldsymbol{\xi} = (\xi, \eta) = (\xi^1, \xi^2) = [-1, 1]^2$, local to an element. Transformation of Equation (5) into a local curvilinear coordinate system results in

$$\mathbf{U}_{t}(\xi,\eta,t) + \frac{1}{J} \left(\frac{\partial \tilde{\mathbf{F}}^{1}(\xi,\eta,t)}{\partial \xi} + \frac{\partial \tilde{\mathbf{F}}^{2}(\xi,\eta,t)}{\partial \eta} \right) = 0, \tag{6}$$

where $\tilde{\mathbf{F}}^l = \mathbf{F} \cdot J \mathbf{a}^l$, l = 1, 2, is a scaled contravariant component of the vector \mathbf{F} , \mathbf{a}^l is the contravariant basis vector, and J is the determinant of the Jacobian matrix,

$$J = \begin{vmatrix} \frac{\partial x}{\partial \xi} & \frac{\partial x}{\partial \eta} \\ \frac{\partial y}{\partial \xi} & \frac{\partial y}{\partial \eta} \end{vmatrix}, \tag{7}$$

and $\mathbf{U}_t = \partial \mathbf{U}/\partial t$ [9]. Equation (6) is subsequently cast into a weak form by taking an inner product with the Lagrange test function $\phi_{ij}(\xi,\eta) = l_i(\xi)l_j(\eta)$, where $l_i(\xi)$, $l_j(\eta)$ are 1D Lagrange basis functions that perform interpolation using Gauss-Lobatto-Legendre (GLL) points (ξ_n,η_m) in the corresponding direction, such that $l_i(\xi_n) = \delta_{in}$, $l_j(\eta_m) = \delta_{jm}$, δ_{in} , δ_{jm} are the Kronecker delta functions. The weak form of (6) is thus given as follows,

$$(\mathbf{U}_t, \phi_{ij}) + \frac{1}{J} \left((\frac{\partial \tilde{\mathbf{F}}^1}{\partial \xi} + \frac{\partial \tilde{\mathbf{F}}^2}{\partial \eta}), \phi_{ij} \right) = 0.$$
 (8)

Multiplying both sides of Equation (8) by J and writing out the inner products as the double integrals over the computational domain, one obtains

$$J\int_{-1}^{1}\int_{-1}^{1}\mathbf{U}_{t}\phi_{ij}d\xi d\eta + \int_{-1}^{1}\int_{-1}^{1}\frac{\partial\tilde{\mathbf{F}}^{1}}{\partial\xi}\phi_{ij}d\xi d\eta + \int_{-1}^{1}\int_{-1}^{1}\frac{\partial\tilde{\mathbf{F}}^{2}}{\partial\eta}\phi_{ij}d\xi d\eta = 0. \tag{9}$$

For the first term on the left hand side of Equation (9), Gauss Lobatto Legendre quadrature is applied to discretize the integral,

$$J\int_{-1}^{1}\int_{-1}^{1}\mathbf{U}_{t}(\xi,\eta,t)\phi_{ij}d\xi d\eta = J\sum_{n=1}^{N}\sum_{m=1}^{N}\mathbf{U}_{t}(\xi_{n},\eta_{m},t)l_{i}(\xi_{n})l_{j}(\eta_{m})w_{n}w_{m},$$
(10)

where w_n , w_m are the quadrature weights. Only when i = n and j = m, the discrete product of two Lagrange basis functions is non-zero, thus

$$J \int_{-1}^{1} \int_{-1}^{1} \mathbf{U}_{t}(\xi, \eta, t) \phi_{ij} d\xi d\eta = J \mathbf{U}_{t}(\xi_{i}, \eta_{j}, t) w_{i} w_{j}. \tag{11}$$

We take the second integral by parts, then discretize the integrals with the Gauss Lobatto Legendre quadrature rule,

$$\int_{-1}^{1} \int_{-1}^{1} \frac{\partial \tilde{\mathbf{F}}^{1}}{\partial \xi} \phi_{ij} d\xi d\eta = \int_{-1}^{1} \left[(\tilde{\mathbf{F}}^{1} \phi_{ij})|_{\xi=-1}^{1} - \int_{-1}^{1} \tilde{\mathbf{F}}^{1} \frac{\partial \phi_{ij}}{\partial \xi} d\xi \right] d\eta$$

$$= \int_{-1}^{1} \left[\tilde{\mathbf{F}}^{1}(1, \eta, t) l_{i}(1) l_{j}(\eta) - \tilde{\mathbf{F}}^{1}(-1, \eta, t) l_{i}(-1) l_{j}(\eta) \right] d\eta - \int_{-1}^{1} \int_{-1}^{1} \tilde{\mathbf{F}}^{1} l'_{i}(\xi) l_{j}(\eta) d\xi d\eta$$

$$= \sum_{n=1}^{N} \left[\tilde{\mathbf{F}}^{1}(\xi_{N}, \eta_{n}, t) l_{i}(\xi_{N}) l_{j}(\eta_{n}) - \tilde{\mathbf{F}}^{1}(\xi_{1}, \eta_{n}, t) l_{i}(\xi_{1}) l_{j}(\eta_{n}) \right] w_{n} - \sum_{n=1}^{N} \sum_{m=1}^{N} \tilde{\mathbf{F}}^{1} l'_{i}(\xi_{n}) l_{j}(\eta_{m}) w_{n} w_{m}$$

$$= \left[\tilde{\mathbf{F}}^{1}(\xi_{N}, \eta_{j}, t) l_{i}(\xi_{N}) w_{j} - \tilde{\mathbf{F}}^{1}(\xi_{1}, \eta_{j}, t) l_{i}(\xi_{1}) w_{j} \right] - \sum_{n=1}^{N} \tilde{\mathbf{F}}^{1}(\xi_{n}, \eta_{j}, t) l'_{i}(\xi_{n}) w_{n} w_{j}.$$
(12)

We can do the same to the last integral in Equation (9) and get

$$\int_{1}^{1} \int_{1}^{1} \frac{\partial \tilde{\mathbf{F}}^{2}}{\partial \eta} \phi_{ij} d\xi d\eta = \left[\tilde{\mathbf{F}}^{2}(\xi_{i}, \eta_{N}, t) l_{j}(\eta_{N}) w_{i} - \tilde{\mathbf{F}}^{2}(\xi_{i}, \eta_{1}, t) l_{j}(\eta_{1}) w_{i} \right] - \sum_{m=1}^{N} \tilde{\mathbf{F}}^{2}(\xi_{i}, \eta_{m}, t) l'_{j}(\eta_{m}) w_{m} w_{i}.$$
(13)

Then Equation (9) becomes

$$J\mathbf{U}_{t}(\xi_{i},\eta_{j},t) + \left[\frac{\tilde{\mathbf{F}}^{1}(1,\eta_{j},t)l_{i}(1)}{w_{i}} - \frac{\tilde{\mathbf{F}}^{1}(-1,\eta_{j},t)l_{i}(-1)}{w_{i}}\right] - \sum_{n=1}^{N} \frac{\tilde{\mathbf{F}}^{1}(\xi_{n},\eta_{j},t)l'_{i}(\xi_{n})w_{n}}{w_{i}},$$

$$+ \left[\frac{\tilde{\mathbf{F}}^{2}(\xi_{i},1,t)l_{j}(1)}{w_{j}} - \frac{\tilde{\mathbf{F}}^{2}(\xi_{i},-1,t)l_{j}(-1)}{w_{j}}\right] - \sum_{m=1}^{N} \frac{\tilde{\mathbf{F}}^{2}(\xi_{i},\eta_{m},t)l'_{j}(\eta_{m})w_{m}}{w_{j}} = 0,$$
(14)

where the terms in the square brackets are the surface fluxes across the element boundaries, and the terms in the sum operators are the volume contributions. Note that, e.g., $l_i(1)$ is only non-zero when i = N, i.e. the surface fluxes only appear for the points that lie at the element boundaries, which is expected.

In Discontinuous Galerkin methods, the fluxes at the element boundaries are not calculated directly from the interface grid point values, but are replaced by the fluxes $\tilde{\mathbf{F}}^{*l}$, which are obtained using a numerical solution of a locally one-dimensional Riemann problem [45], such as

$$J\mathbf{U}_{t}(\xi_{i},\eta_{j},t) + \left[\frac{\tilde{\mathbf{F}}^{*1}(1,\eta_{j},t)l_{i}(1)}{w_{i}} - \frac{\tilde{\mathbf{F}}^{*1}(-1,\eta_{j},t)l_{i}(-1)}{w_{i}}\right] - \sum_{n=1}^{N} \frac{\tilde{\mathbf{F}}^{1}(\xi_{n},\eta_{j},t)l'_{i}(\xi_{n})w_{n}}{w_{i}} + \left[\frac{\tilde{\mathbf{F}}^{*2}(\xi_{i},1,t)l_{j}(1)}{w_{j}} - \frac{\tilde{\mathbf{F}}^{*2}(\xi_{i},-1,t)l_{j}(-1)}{w_{j}}\right] - \sum_{m=1}^{N} \frac{\tilde{\mathbf{F}}^{2}(\xi_{i},\eta_{m},t)l'_{j}(\eta_{m})w_{m}}{w_{j}} = 0.$$
(15)

This is done in order to retain stability of the numerical method in hyperbolic systems, where the direction of the propagation of information along the characteristic lines must be taken into account. A Riemann flux scheme, namely, the local Lax-Friedrichs (LLF) flux [46], for calculating the fluxes $\tilde{\mathbf{F}}^{*l}$, is implemented and tested in the current work. The local Lax-Friedrichs flux is divided into non-dissipative and dissipative parts,

$$\tilde{\mathbf{F}}_{LF}^{*l}(\mathbf{U}^{+}, \mathbf{U}^{-}) = \underbrace{\frac{1}{2} \left(\tilde{\mathbf{F}}^{+l} + \tilde{\mathbf{F}}^{-l} \right)}_{\text{Non-dissipative}} - \underbrace{\frac{1}{2} \lambda_{max} \left(\mathbf{U}^{+} - \mathbf{U}^{-} \right) |J\mathbf{a}^{l}|}_{\text{Dissipative}}, \tag{16}$$

where

$$\lambda_{max} = \max\left(c^{+} + |\mathbf{u}^{+} \cdot \hat{\mathbf{n}}^{l}|, c^{-} + |\mathbf{u}^{-} \cdot \hat{\mathbf{n}}^{l}|\right),\tag{17}$$

c is the speed of sound, \dot{t} denotes a boundary gridpoint value taken from the element adjacent to the interface in the increasing ξ^l coordinate direction, while \dot{t} denotes a boundary gridpoint value taken from the element adjacent to the interface in the decreasing ξ^l coordinate direction, and $\hat{\mathbf{n}}^l = (n_1^l, n_2^l)^T$ is the interface unit normal vector pointing from the element \dot{t} to the element (i.e., in the direction of increasing \dot{t}). It is seen that the dissipative portion depends on the local maximum characteristic wave speed between the two sides of the interface λ_{max} , as well as the jump of the conserved variables at the interface. The non-dissipative portion is replaced by the Pirozzoli flux [28] for its kinetic energy preserving property,

$$\frac{1}{2} \left(\tilde{\mathbf{F}}^{+l} + \tilde{\mathbf{F}}^{-l} \right) \approx \tilde{\mathbf{F}}_{PI}^{l} (\mathbf{U}^{+}, \mathbf{U}^{-}). \tag{18}$$

The Pirozzoli flux can be generally expressed as follows,

$$\tilde{\mathbf{F}}_{PI}^{l}(\mathbf{U}_{1}, \mathbf{U}_{2}) = \begin{pmatrix}
\{\{\rho\}\}\{\{\mathbf{u}\}\} \\
\{\{\rho\}\}\{\{\mathbf{u}\}\} \\
\{\{\rho\}\}\{\{\mathbf{e} + \frac{p}{\rho}\}\}\{\{\mathbf{u}^{T}\}\}
\end{pmatrix} J\mathbf{a}^{l}, \tag{19}$$

where $\{\{v\}\}=\frac{1}{2}\,(v_1+v_2)$. For all the test cases in this paper, the interface flux is evaluated using the Pirozzoli flux with a LLF-type dissipation term.

Boundary conditions are imposed weakly when calculating the surface fluxes. At a boundary surface, since there is no neighbor element, \mathbf{U}^{\pm} is replaced by \mathbf{U}_b for Dirichlet boundary conditions, where \mathbf{U}_b is the solution vector at the boundary, or \mathbf{U}^{\mp} for zero-gradient Neumann boundary conditions.

The volume contributions in the standard DGSEM are calculated directly using the conserved variables at each GLL point. Since polynomials are used to approximate the solutions, aliasing error occurs when estimating the non-linear terms, especially in the volume contributions. Filtering techniques [25,1] or over-integration method [22,9] may be introduced to reduce the aliasing error. For filtering, additional parameters have to be determined, which makes it difficult to find a set of parameters that works for most of the cases. In terms of over-integration, it is computationally expensive. Not to mention that the "3/2 rule" loses its theoretical foundation in application to compressible flows [24,47]. To circumvent these issues, we have implemented an alternative method for calculating the volume contributions based on a split-form DGSEM with summation-by-parts properties [7], which is introduced in the next section.

2.2. Split form DGSEM with SBP operator

Previous studies [7] have shown that using the split-form DGSEM-SBP and a differencing formulation for the volume contributions leads to a class of methods that are energy stable or entropy stable in a discrete sense showing superior stability properties in a continuous framework. In the work of Gassner et al. [7], the method was described in a strong form. In order to keep consistent with the previous section, we have derived the formulation in a weak form. We start from the following equation,

$$\int_{-1}^{1} l_n(\xi) l_i'(\xi) d\xi = [l_n(\xi) l_i(\xi)]_{-1}^{1} - \int_{-1}^{1} l_n'(\xi) l_i(\xi) d\xi$$
(20)

Gauss Lobatto Legendre quadrature rule is employed to discretize the integrals, so that the integration-by-part operation is transferred into a summation-by-part operation,

$$\sum_{k=1}^{N} l_n(\xi_k) l_i'(\xi_k) w_k = l_n(\xi_N) l_i(\xi_N) - l_n(\xi_1) l_i(\xi_1) - \sum_{k=1}^{N} l_n'(\xi_k) l_i(\xi_k) w_k.$$
(21)

Due to the cardinal property of the Lagrange basis functions, $l_i(\xi_k) = \delta_{ik}$, we have

$$l'_{i}(\xi_{n})w_{n} = l_{n}(\xi_{N})l_{i}(\xi_{N}) - l_{n}(\xi_{1})l_{i}(\xi_{1}) - l'_{n}(\xi_{i})w_{i}.$$
(22)

This allows us to replace the term $l_i'(\xi_n)w_n$ in the definition of the volume contribution associated with the $\tilde{\mathbf{F}}^1$ flux in (14) with the corresponding SBP operator. The volume contribution term then becomes

$$\sum_{n=1}^{N} \frac{\tilde{\mathbf{F}}^{1}(\xi_{n}, \eta_{j}, t) l_{i}'(\xi_{n}) w_{n}}{w_{i}} = \frac{1}{w_{i}} \sum_{n=1}^{N} \tilde{\mathbf{F}}^{1}(\xi_{n}, \eta_{j}, t) \left[l_{n}(\xi_{N}) l_{i}(\xi_{N}) - l_{n}(\xi_{1}) l_{i}(\xi_{1}) \right] - \frac{1}{w_{i}} \sum_{n=1}^{N} \tilde{\mathbf{F}}^{1}(\xi_{n}, \eta_{j}, t) l_{n}'(\xi_{i}) w_{i}$$

$$= \frac{1}{w_{i}} \left[\tilde{\mathbf{F}}^{1}(\xi_{N}, \eta_{j}, t) l_{i}(\xi_{N}) - \tilde{\mathbf{F}}^{1}(\xi_{1}, \eta_{j}, t) l_{i}(\xi_{1}) \right] - \frac{1}{w_{i}} \sum_{n=1}^{N} \tilde{\mathbf{F}}^{1}(\xi_{n}, \eta_{j}, t) l_{n}'(\xi_{i}) w_{i}. \tag{23}$$

We note that due to the SBP property, the strong form DGSEM and the weak form DGSEM are algebraically equivalent. Considering the last term in Equation (23), it was shown in [48,6,7] that, due to the SBP properties of the differentiation matrix $D = [l'_i(\xi_i)]$, it can be written in the following, telescopic flux form,

$$\frac{1}{w_i} \sum_{n=1}^{N} \tilde{\mathbf{F}}^1(\xi_n, \eta_j, t) l'_n(\xi_i) w_i = \frac{\Delta \tilde{\tilde{\mathbf{F}}}^1(\xi_i, \eta_j, t)}{w_i}, \tag{24}$$

where $\Delta \bar{\tilde{\mathbf{F}}}^1(\xi_i, \eta_j, t) = \bar{\tilde{\mathbf{F}}}^1(\xi_{i+1}, \eta_j, t) - \bar{\tilde{\mathbf{F}}}^1(\xi_i, \eta_j, t)$ is a differencing operator. This form is the key to ensure conservation. Another important result proven in [6,48] allows to extend a telescopic flux form to a high-order approximation as

$$\frac{\Delta \tilde{\mathbf{F}}^{1}(\xi_{i}, \eta_{j}, t)}{w_{i}} = \frac{2}{w_{i}} \sum_{n=1}^{N} \tilde{\mathbf{F}}^{1\#} \left(\mathbf{U}(\xi_{n}, \eta_{j}, t), \mathbf{U}(\xi_{i}, \eta_{j}, t) \right) l'_{n}(\xi_{i}) w_{i}, \tag{25}$$

where $\tilde{\mathbf{F}}^{l\#}$ is a suitable two-point flux function. Gassner et al. [7] showed that fluxes $\tilde{\mathbf{F}}^{l\#}$ written in a so-called split form preserve a high-order discretization, while some specific flux choices can additionally lead to a preservation of either a kinetic energy [28,27], or an entropy [49,50]. Note that it is not trivial to obtain a formulation that conserves both kinetic energy and entropy. While the split-form flux of Chandrashekar [50] formally is supposed to yield both kinetic energy and entropy conservation, numerical tests show that it dissipates kinetic energy more than some other flux schemes that are not formally kinetic-energy preserving, such as [29]. This might be due to a pressure discretization [7]. In the current work, a Pirozzoli split-form flux formulation [28], given by Equation (19), is used to approximate $\tilde{\mathbf{F}}^{l\#}$. This yields a kinetic energy preserving scheme with strong stability properties.

preserving scheme with strong stability properties. Plugging Equation (24) and (25) with $\tilde{\mathbf{F}}^{l}$ replaced by the Pirozzoli flux $\tilde{\mathbf{F}}_{Pl}^{l}$ into Equation (23) yields

$$\sum_{n=1}^{N} \frac{\tilde{\mathbf{F}}^{1} l_{i}'(\xi_{n}) w_{n}}{w_{i}} = \frac{1}{w_{i}} \left[\tilde{\mathbf{F}}^{1}(\xi_{N}, \eta_{j}, t) l_{i}(\xi_{N}) - \tilde{\mathbf{F}}^{1}(\xi_{1}, \eta_{j}, t) l_{i}(\xi_{1}) \right] - 2 \sum_{n=1}^{N} \tilde{\mathbf{F}}^{1}_{PI}(\mathbf{U}(\xi_{n}, \eta_{j}, t), \mathbf{U}(\xi_{i}, \eta_{j}, t)) l_{n}'(\xi_{i}). \tag{26}$$

Similarly, we have

$$\sum_{m=1}^{N} \frac{\tilde{\mathbf{F}}^{2} l'_{j}(\eta_{m}) w_{m}}{w_{j}} = \frac{1}{w_{j}} \left[\tilde{\mathbf{F}}^{2}(\xi_{i}, \eta_{N}, t) l_{j}(\eta_{N}) - \tilde{\mathbf{F}}^{2}(\xi_{i}, \eta_{1}, t) l_{j}(\eta_{1}) \right] - 2 \sum_{m=1}^{N} \tilde{\mathbf{F}}^{2}_{PI}(\mathbf{U}(\xi_{i}, \eta_{m}, t), \mathbf{U}(\xi_{i}, \eta_{j}, t)) l'_{m}(\eta_{j}). \quad (27)$$

Plugging Equation (26) and (27) back into Equation (14), with $\xi_N = \eta_N = 1$ and $\xi_1 = \eta_1 = -1$, we get the SBP form of the discretized two-dimensional governing equations,

$$J\mathbf{U}_{t} + \frac{l_{i}(1)}{w_{i}} \left[\tilde{\mathbf{F}}^{1*}(1, \eta_{j}, t) - \tilde{\mathbf{F}}^{1}(1, \eta_{j}, t) \right] - \frac{l_{i}(-1)}{w_{i}} \left[\tilde{\mathbf{F}}^{1*}(-1, \eta_{j}, t) - \tilde{\mathbf{F}}^{1}(-1, \eta_{j}, t) \right]$$

$$+ 2 \sum_{n=1}^{N} \tilde{\mathbf{F}}_{Pl}^{1} (\mathbf{U}(\xi_{n}, \eta_{j}, t), \mathbf{U}(\xi_{i}, \eta_{j}, t)) l'_{n}(\xi_{i})$$

$$+ \frac{l_{j}(1)}{w_{j}} \left[\tilde{\mathbf{F}}^{2*}(\xi_{i}, 1, t) - \tilde{\mathbf{F}}^{2}(\xi_{i}, 1, t) \right] - \frac{l_{j}(-1)}{w_{j}} \left[\tilde{\mathbf{F}}^{2*}(\xi_{i}, -1, t) - \tilde{\mathbf{F}}^{2}(\xi_{i}, -1, t) \right]$$

$$+ 2 \sum_{m=1}^{N} \tilde{\mathbf{F}}_{Pl}^{2} (\mathbf{U}(\xi_{i}, \eta_{m}, t), \mathbf{U}(\xi_{i}, \eta_{j}, t)) l'_{m}(\eta_{j})$$

$$= 0,$$

$$(28)$$

where $\tilde{\mathbf{F}}_l^*$ denote Riemann fluxes calculated via Equation (16), and $\tilde{\mathbf{F}}_l$ are computed directly using the interface GLL points. So far we have introduced the split formulation, SBP operator and the volume flux differencing formulation into DGSEM. The solver is ready for most continuous problems. However, for discontinuous problems, especially those with shocks, additional stabilizing techniques are needed.

2.3. Viscous regularization of the Euler equation

In this section, we are applying viscous regularization to the governing equations to stabilize the solution near discontinuities. Diffusion terms are added to the right-hand-side of Equation (1),

$$\frac{\partial \mathbf{U}}{\partial t} + \nabla \cdot \mathbf{F} = \nabla \cdot \mathbf{q},\tag{29}$$

$$\mathbf{q} = \tilde{\mathbf{v}} \, \nabla \mathbf{U},\tag{30}$$

where $\mathbf{q} = (\mathbf{q}_1, \mathbf{q}_2)$ for two-dimensional cases, and \tilde{v} is the artificial viscosity. Casting Equations (29), (30) into curvilinear coordinates, we have (see, e.g., [9])

$$\frac{\partial \mathbf{U}(\xi,\eta,t)}{\partial t} + \frac{1}{J} \left(\frac{\partial \tilde{\mathbf{F}}^{1}(\xi,\eta,t)}{\partial \xi} + \frac{\partial \tilde{\mathbf{F}}^{2}(\xi,\eta,t)}{\partial \eta} \right) = \frac{1}{J} \left(\frac{\partial \tilde{\mathbf{q}}^{1}(\xi,\eta,t)}{\partial \xi} + \frac{\partial \tilde{\mathbf{q}}^{2}(\xi,\eta,t)}{\partial \eta} \right), \tag{31}$$

$$\mathbf{q}(\xi,\eta,t) = \frac{\tilde{\nu}}{J} \left(\frac{\partial \mathbf{U}(\xi,\eta,t)}{\partial \xi} J \mathbf{a}^1 + \frac{\partial \mathbf{U}(\xi,\eta,t)}{\partial \eta} J \mathbf{a}^2 \right), \tag{32}$$

where $\tilde{\mathbf{q}}^l = \mathbf{q} \cdot J \mathbf{a}^l$.

An entropy-residual based shock indicator [37] is adopted to calculate $\tilde{\nu}$ in the above equation. The shock indicator should be activated only in the vicinity of discontinuities to avoid adding extra dissipation in the smooth portions of the solution. The entropy residual at a GLL point (ξ_i, η_i) in an element Ω_e is calculated by the following procedure,

$$R_{s}(\xi_{i}, \eta_{j}, t) := \frac{\partial S(\xi_{i}, \eta_{j}, t)}{\partial t} + \tilde{\nabla} \cdot \left[S(\xi_{i}, \eta_{j}, t) \mathbf{u}(\xi_{i}, \eta_{j}, t) \right],$$

$$S(\xi_{i}, \eta_{j}, t) = \frac{\rho(\xi_{i}, \eta_{j}, t)}{\gamma - 1} \log \left(\frac{p(\xi_{i}, \eta_{j}, t)}{\rho^{\gamma}(\xi_{i}, \eta_{j}, t)} \right),$$
(33)

where γ is the ratio of a specific heat coefficient at a constant pressure to that of a constant density, and $\tilde{\nabla}$ is the divergence operator in curvilinear coordinates as defined previously, $\tilde{\nabla} \cdot [S\mathbf{u}] = 1/J \sum_l \partial (S\mathbf{u} \cdot J\mathbf{a}^l)/\partial \xi^l$. Following the method in [37], the residual-based kinematic viscosity is expressed as

$$\nu^*(\xi_i, \eta_j, t) = c^* \left(\frac{h_e}{N - 1}\right)^2 \frac{|R_s(\xi_i, \eta_j, t)|}{\|S(\xi_i, \eta_j, t) - \bar{S}(t)\|_{\infty}},\tag{34}$$

where c^* is the first empirical parameter of the scheme, h_e is the characteristic length of an element, the bar over S denotes the average of S in an element, $\|\cdot\|_{\infty}$ is the L_{∞} -norm over the whole domain. Then the maximum viscosity used to bound $\tilde{\nu}$ is obtained as.

$$\nu_{max}(\xi_i, \eta_j, t) = c_{max} \frac{h_e}{N - 1} \max_{k, l = 1, 2, \dots, N} \lambda(\xi_k, \eta_l, t), \tag{35}$$

$$\lambda(\xi_i, \eta_i, t) = c(\xi_i, \eta_i, t) + |\mathbf{u}(\xi_i, \eta_i, t)|,\tag{36}$$

where c_{max} is the second empirical parameter of the scheme, and the maximum in the right-hand side of Equation (35) is taken over an element. Finally, we have

$$\tilde{\nu} = \mathcal{P} \mathcal{F}(\min(\nu^*, \nu_{max})) \Theta, \tag{37}$$

where \mathcal{P} is the third empirical parameter of the scheme that satisfies $\mathcal{P} \leq 1$, and \mathcal{F} is a smoothing function [37] defined as follows:

$$\mathcal{F}(\nu_{i,j}) = \frac{1}{8} \left(4\nu_{i,j} + \nu_{i-1,j} + \nu_{i+1,j} + \nu_{i,j-1} + \nu_{i,j+1} \right), \tag{38}$$

where $v_{i,j} = v(\xi_i, \eta_j)$ with i, j = 1, 2, ..., N. Variables on the boundaries are defined in a symmetric way, as: $v_{0,j} = v_{2,j}$, $v_{N,j} = v_{N-2,j}$, $v_{i,0} = v_{i,2}$, $v_{i,N} = v_{i,N-2}$. The function Θ in Equation (37) is a modified Ducros sensor defined as follows [43],

$$\Theta = \frac{(\nabla \cdot \mathbf{u})^2}{(\nabla \cdot \mathbf{u})^2 + \beta (|\mathbf{u}|/L_0)^2 + \epsilon},\tag{39}$$

where $L_0 = h_e/(N-1)$ is the length scale, $\epsilon = 10^{-15}$ is a small number to avoid being divided by zero, β can be regarded as the fourth empirical parameter of the scheme, but is set to 0.01 here according to [43]. By now, we have determined the value of the artificial viscosity $\tilde{\nu}$.

At this point, we turn to the gradients of the conserved variables and to the weak form of Equation (32). Recognizing that

$$\tilde{\mathbf{q}}_{m} = \tilde{v} J \frac{\partial U(\xi, \eta, t)}{\partial \xi^{m}}, \tag{40}$$

is a scaled covariant component of the vector \mathbf{q} , $\tilde{\mathbf{q}}_m = \mathbf{q} \cdot J \mathbf{a}_m$, \mathbf{a}_m is the covariant basis vector, we can write a weak form for $\tilde{\mathbf{q}}_m$ as

$$\frac{1}{\tilde{\nu}J}\int_{-1}^{1}\int_{-1}^{1}\tilde{\mathbf{q}}_{m}(\xi,\eta,t)\phi_{ij}d\xi d\eta = \int_{-1}^{1}\int_{-1}^{1}\frac{\partial\mathbf{U}(\xi,\eta,t)}{\partial\xi^{m}}\phi_{ij}d\xi d\eta. \tag{41}$$

Taking, e.g., m = 1 and applying the same procedure as in Equation (12) to Equation (41), we obtain

$$\frac{1}{\tilde{\nu}J}\tilde{\mathbf{q}}_{1}(\xi_{i},\eta_{j},t)w_{i}w_{j} = \left[\mathbf{U}(1,\eta_{j},t)l_{i}(1)w_{j} - \mathbf{U}(-1,\eta_{j},t)l_{i}(-1)w_{j}\right] - \sum_{n=1}^{N}\mathbf{U}(\xi_{n},\eta_{j},t)l_{i}'(\xi_{n})w_{n}w_{j}.$$
(42)

Following [51], the element boundary values $\mathbf{U}(\pm 1, \eta_j, t)$ in the square brackets of Equation (42) are replaced by their averaged values between the adjacent elements $\mathbf{U}^*(\pm 1, \eta_j, t)$,

$$\frac{1}{\tilde{\nu}J}\tilde{\mathbf{q}}_{1}(\xi_{i},\eta_{j},t)w_{i}w_{j} = \left[\mathbf{U}^{*}(1,\eta_{j},t)l_{i}(1)w_{j} - \mathbf{U}^{*}(-1,\eta_{j},t)l_{i}(-1)w_{j}\right] - \sum_{n=1}^{N}\mathbf{U}(\xi_{n},\eta_{j},t)l'_{i}(\xi_{n})w_{n}w_{j},\tag{43}$$

where

$$\mathbf{U}^* = \frac{1}{2} \left(\mathbf{U} + \mathbf{U}^{neighbor} \right), \tag{44}$$

and $\mathbf{U}^{neighbor}$ is the value obtained at the boundary point of the neighboring element across the interface. As suggested in [51], the jump across the interface is introduced directly into the discretization as

$$\mathbf{U}^{**} = \frac{1}{2} \left(\mathbf{U}^{neighbor} - \mathbf{U} \right), \tag{45}$$

yielding

$$\mathbf{U}^* = \mathbf{U}^{**} + \mathbf{U},\tag{46}$$

which transforms Equation (43) into

$$\frac{1}{\tilde{\nu}J}\tilde{\mathbf{q}}_{1}(\xi_{i},\eta_{j},t)w_{i}w_{j} = \left[\mathbf{U}^{**}(1,\eta_{j},t)l_{i}(1)w_{j} - \mathbf{U}^{**}(-1,\eta_{j},t)l_{i}(-1)w_{j}\right]
+ \left[\mathbf{U}(1,\eta_{j},t)l_{i}(1)w_{j} - \mathbf{U}(-1,\eta_{j},t)l_{i}(-1)w_{j}\right]
- \sum_{n=1}^{N}\mathbf{U}(\xi_{n},\eta_{j},t)l_{i}'(\xi_{n})w_{n}w_{j}.$$
(47)

Then we apply the SBP operation given by Equation (22) and the cardinal property of the Lagrange basis functions to the last term of Equation (47),

$$\sum_{n=1}^{N} \mathbf{U}(\xi_{n}, \eta_{j}, t) l'_{i}(\xi_{n}) w_{n} w_{j} = \sum_{n=1}^{N} \mathbf{U}(\xi_{n}, \eta_{j}, t) w_{j} \left[l_{n}(\xi_{N}) l_{i}(\xi_{N}) - l_{n}(\xi_{1}) l_{i}(\xi_{1}) - l'_{n}(\xi_{i}) w_{i} \right]
= \mathbf{U}(1, \eta, j, t) l_{i}(1) w_{j} - \mathbf{U}(-1, \eta_{j}, t) l_{i}(-1) w_{j} - \sum_{n=1}^{N} \mathbf{U}(\xi_{n}, \eta_{j}, t) l'_{n}(\xi_{i}) w_{i} w_{j}.$$
(48)

After plugging Equation (48) into (47), we have

$$\frac{1}{\tilde{\nu}J}\tilde{\mathbf{q}}_{1}(\xi_{i},\eta_{j},t)w_{i}w_{j} = \left[\mathbf{U}^{**}(1,\eta_{j},t)l_{i}(1)w_{j} - \mathbf{U}^{**}(-1,\eta_{j},t)l_{i}(-1)w_{j}\right] + \sum_{n=1}^{N}\mathbf{U}(\xi_{n},\eta_{j},t)l_{n}'(\xi_{i})w_{i}w_{j}. \tag{49}$$

Dividing by $w_i w_j$ on both sides of Equation (49), we get

$$\frac{1}{\tilde{\nu}J}\tilde{\mathbf{q}}_{1}(\xi_{i},\eta_{j},t) = \frac{1}{w_{i}}\left[\mathbf{U}^{**}(1,\eta_{j},t)l_{i}(1) - \mathbf{U}^{**}(-1,\eta_{j},t)l_{i}(-1)\right] + \sum_{n=1}^{N}\mathbf{U}(\xi_{n},\eta_{j},t)l_{n}'(\xi_{i}). \tag{50}$$

Similarly, for the second scaled covariant component of \mathbf{q} , we can write

$$\frac{1}{\tilde{\nu}J}\tilde{\mathbf{q}}_{2}(\xi_{i},\eta_{j},t) = \frac{1}{w_{j}}\left[\mathbf{U}^{**}(\xi_{i},1,t)l_{j}(1) - \mathbf{U}^{**}(\xi_{i},-1,t)l_{j}(-1)\right] + \sum_{m=1}^{N}\mathbf{U}(\xi_{i},\eta_{m},t)l'_{m}(\eta_{j}). \tag{51}$$

Scaled contravariant components of the vector \mathbf{q} , $\tilde{\mathbf{q}}^l$, appearing in the right-hand side of Equation (31), can be obtained from the scaled covariant components $\tilde{\mathbf{q}}_m$ via

$$\tilde{\mathbf{q}}^l = g^{ml} \tilde{\mathbf{q}}_m, \tag{52}$$

where $g^{ml} = \mathbf{a}^m \cdot \mathbf{a}^l$ is the contravariant metric tensor [9].

So far, we have presented a discrete approximation of Equation (32). Now we can move on to Equation (31) and discretize it in the same way as was done for Equation (6), by treating the divergence of \mathbf{q} in the right-hand side of (6) analogously to the divergence of \mathbf{F} , see Equation (12), (13). The final form of the split DGSEM-SBP discretization of Equation (31) with viscous regularization reads

$$J\mathbf{U}_{t} + \frac{l_{i}(1)}{w_{i}} \left[\tilde{\mathbf{F}}^{1*}(1, \eta_{j}, t) - \tilde{\mathbf{F}}^{1}(1, \eta_{j}, t) \right] - \frac{l_{i}(-1)}{w_{i}} \left[\tilde{\mathbf{F}}^{1*}(-1, \eta_{j}, t) - \tilde{\mathbf{F}}^{1}(-1, \eta_{j}, t) \right]$$

$$+ 2 \sum_{n=1}^{N} \tilde{\mathbf{F}}_{PI}^{1} (\mathbf{U}(\xi_{n}, \eta_{j}, t), \mathbf{U}(\xi_{i}, \eta_{j}, t)) l_{n}'(\xi_{i})$$

$$+ \frac{l_{j}(1)}{w_{j}} \left[\tilde{\mathbf{F}}^{2*}(\xi_{i}, 1, t) - \tilde{\mathbf{F}}^{2}(\xi_{i}, 1, t) \right] - \frac{l_{j}(-1)}{w_{j}} \left[\tilde{\mathbf{F}}^{2*}(\xi_{i}, -1, t) - \tilde{\mathbf{F}}^{2}(\xi_{i}, -1, t) \right]$$

$$+ 2 \sum_{m=1}^{N} \tilde{\mathbf{F}}_{PI}^{2} (\mathbf{U}(\xi_{i}, \eta_{m}, t), \mathbf{U}(\xi_{i}, \eta_{j}, t)) l_{m}'(\eta_{j})$$

$$= \left[\frac{l_{i}(1)}{w_{i}} \tilde{\mathbf{q}}^{1*}(1, \eta_{j}, t) - \frac{l_{i}(-1)}{w_{i}} \tilde{\mathbf{q}}^{1*}(-1, \eta_{j}, t) \right] - \sum_{n=1}^{N} \tilde{\mathbf{q}}^{1}(\xi_{i}, \eta_{j}, t) l_{i}'(\xi_{n}) \frac{w_{n}}{w_{i}}$$

$$+ \left[\frac{l_{j}(1)}{w_{j}} \tilde{\mathbf{q}}^{2*}(\xi_{i}, 1, t) - \frac{l_{j}(-1)}{w_{j}} \tilde{\mathbf{q}}^{2*}(\xi_{i}, -1, t) \right] - \sum_{m=1}^{N} \tilde{\mathbf{q}}^{2}(\xi_{i}, \eta_{j}, t) l_{j}'(\eta_{m}) \frac{w_{m}}{w_{j}} .$$

$$(53)$$

We approximate the interface flux $\tilde{\mathbf{q}}^{l*}$ as

$$\tilde{\mathbf{q}}^{l*} = \frac{1}{2} \left(\tilde{\mathbf{q}}^{l} + \tilde{\mathbf{q}}^{l,neighbor} \right) - \alpha \frac{C(N)}{L_{0}} \left(\mathbf{U} - \mathbf{U}^{neighbor} \right) |J\mathbf{a}^{l}|, \tag{54}$$

where $C(N) = N^2/2$ [52], $L_0 = h_e/(N-1)$, α equals to 0 or 1 to turn off or on the penalty term, which is only needed for cases with strong shocks, such as the 2D Riemann problem case 3 considered here. At this stage, we have discretized all the spatial terms.

2.4. Time integration

We first derive the semi-discrete form for the time integration. Equation (53) can be rewritten as

$$\mathbf{U}_{t}(\xi_{i},\eta_{j},t) = \operatorname{Res}\left(\mathbf{U}(\xi_{i},\eta_{j},t)\right),\tag{55}$$

where

$$\operatorname{Res}\left(\mathbf{U}(\xi_{i},\eta_{j},t)\right) = -\frac{l_{i}(1)}{Jw_{i}} \left[\tilde{\mathbf{F}}^{1*}(1,\eta_{j},t) - \tilde{\mathbf{F}}^{1}(1,\eta_{j},t)\right] + \frac{l_{i}(-1)}{Jw_{i}} \left[\tilde{\mathbf{F}}^{1*}(-1,\eta_{j},t) - \tilde{\mathbf{F}}^{1}(-1,\eta_{j},t)\right] \\ -\frac{2}{J} \sum_{n=1}^{N} \tilde{\mathbf{F}}_{Pl}^{1} \left(\mathbf{U}(\xi_{n},\eta_{j},t), \mathbf{U}(\xi_{i},\eta_{j},t)\right) l_{n}'(\xi_{i}) \\ -\frac{l_{j}(1)}{Jw_{j}} \left[\tilde{\mathbf{F}}^{2*}(\xi_{i},1,t) - \tilde{\mathbf{F}}^{2}(\xi_{i},1,t)\right] + \frac{l_{j}(-1)}{Jw_{j}} \left[\tilde{\mathbf{F}}^{2*}(\xi_{i},-1,t) - \tilde{\mathbf{F}}^{2}(\xi_{i},-1,t)\right] \\ -\frac{2}{J} \sum_{m=1}^{N} \tilde{\mathbf{F}}_{Pl}^{2} \left(\mathbf{U}(\xi_{i},\eta_{m},t), \mathbf{U}(\xi_{i},\eta_{j},t)\right) l_{m}'(\eta_{j}) \\ + \frac{1}{J} \left[\frac{l_{i}(1)}{w_{i}} \tilde{\mathbf{q}}^{1*}(1,\eta_{j},t) - \frac{l_{i}(-1)}{w_{i}} \tilde{\mathbf{q}}^{1*}(-1,\eta_{j},t)\right] - \frac{1}{J} \sum_{n=1}^{N} \tilde{\mathbf{q}}^{1}(\xi_{i},\eta_{j},t) l_{i}'(\xi_{n}) \frac{w_{n}}{w_{i}} \\ + \frac{1}{J} \left[\frac{l_{j}(1)}{w_{i}} \tilde{\mathbf{q}}^{2*}(\xi_{i},1,t) - \frac{l_{j}(-1)}{w_{i}} \tilde{\mathbf{q}}^{2*}(\xi_{i},-1,t)\right] - \frac{1}{J} \sum_{n=1}^{N} \tilde{\mathbf{q}}^{2}(\xi_{i},\eta_{j},t) l_{j}'(\eta_{m}) \frac{w_{m}}{w_{i}}.$$
(56)

The third-order strong stability-preserving Runge-Kutta scheme [53] is applied to integrate the equations (55), (56) in time from t^n to t^{n+1} ,

$$\mathbf{U}^{(1)}(\xi_{i},\eta_{j},t^{n}) = \mathbf{U}(\xi_{i},\eta_{j},t^{n}) + \Delta t \operatorname{Res} \left(\mathbf{U}(\xi_{i},\eta_{j},t^{n})\right),
\mathbf{U}^{(2)}(\xi_{i},\eta_{j},t^{n}) = \frac{3}{4}\mathbf{U}(\xi_{i},\eta_{j},t^{n}) + \frac{1}{4}\mathbf{U}^{(1)}(\xi_{i},\eta_{j},t^{n}) + \frac{1}{4}\Delta t \operatorname{Res} \left(\mathbf{U}^{(1)}(\xi_{i},\eta_{j},t^{n})\right),
\mathbf{U}(\xi_{i},\eta_{j},t^{n+1}) = \frac{1}{3}\mathbf{U}(\xi_{i},\eta_{j},t^{n}) + \frac{2}{3}\mathbf{U}^{(2)}(\xi_{i},\eta_{j},t^{n}) + \frac{2}{3}\Delta t \operatorname{Res} \left(\mathbf{U}^{(2)}(\xi_{i},\eta_{j},t^{n})\right).$$
(57)

The time step Δt is bounded by the condition numbers of both the convection and the diffusion parts of the equation in the following expressions,

$$\Delta t < \min(\Delta t_c, \Delta t_d),\tag{58}$$

with

$$\Delta t_{c} \leq C_{c} \min_{i,j=1,2,...,N_{t}} \frac{h_{e}}{(N-1)^{2} \lambda(\xi_{i}, \eta_{j}, t)},$$

$$\Delta t_{d} \leq C_{d} \min_{i,j=1,2,...,N_{t}} \frac{h_{e}^{2}}{(N-1)^{4} \tilde{\nu}(\xi_{i}, \eta_{j}, t)},$$
(59)

where N_t is the total number of GLL points in the whole domain. The coefficients C_c , C_d in Equation (59) must be less than unity for stability. In Equation (59), Δt_c and Δt_d drop with the polynomial orders of $(N-1)^{-2}$ and $(N-1)^{-4}$, respectively, due to a quadratic clustering rule of the GLL points towards the element boundaries [33,9,26]. These conditions can be markedly restrictive, especially in the situation of strong shocks, where higher values of artificial viscosity are needed for stability, and while resolving sharp gradients, where element sizes have to be small. This is the downside of the viscous shock capturing method with the explicit time integration scheme. To assess the time step constraints employed in the following cases, we compute the normalized time step for each test case as

$$CFL = \Delta t \max_{i,j=1,2,\dots,N_t} \left(\left| \frac{\lambda \cdot \mathbf{a}^1}{\int \Delta \xi_i} \right| + \left| \frac{\lambda \cdot \mathbf{a}^2}{\int \Delta \eta_i} \right| \right)$$
 (60)

where $\lambda = (|u| + c, |v| + c)$ is the maximum wave speed calculated locally on GLL points.

Table 1Simulation parameters used in each test case.

Cases	Section	CFL	c*	c _{max}	\mathcal{P}	β	α
Euler vortex, VON	Section 3.1	0.15 - 0.45	10	0.5	0.7	0.01	1
Euler vortex, VOFF	Section 3.1	0.40 - 0.50	0	0	0	0	0
Kelvin-Helmholtz	Section 3.2	0.45 - 0.50	10	0.5	0.7	0.01	0
Sod shocktube	Section 3.3	0.15 - 0.30	10	0.5	0.7	0.01	0
Lax problem	Section 3.4	0.15 - 0.45	10	0.5	0.7	0.01	0
Shu-Osher problem	Section 3.5	0.25 - 0.30	10	0.5	0.7	0.01	0
Mach 3 forward step	Section 3.6	0.20 - 0.35	10	0.5	0.7	0.01	0
Riemann case 3	Section 3.7	0.07 - 0.12	10	0.5	0.7	0.01	1
Riemann case 15	Section 3.8	0.20 - 0.25	10	0.5	0.7	0.01	0

3. Numerical results

Eight problems are presented for the purposes of verification and testing of the developed methodology, as summarized in Table 1. The isentropic Euler vortex problem is used to assess the order of convergence and check long-term stability properties of the method. The 2D inviscid Kelvin-Helmholtz instability is a challenging but shock-free test case. It can quickly get under-resolved and requires additional stabilization techniques beyond the split-form DGSEM. The Sod [54] and Lax shocktube [46] are basic 1D problems to test the numerical resolution of discontinuities. The Shu-Osher problem requires the ability not only to capture shocks, but also to resolve the fine structures [55]. For the Mach 3 step problem, there are interesting physical phenomena to be captured, for example, a bow shock locating upstream of the step, a Mach stem and a contact discontinuity near the upper boundary, as well as the reflecting shocks [56,57]. The subsequent 2D Riemann problems [58,59] focus on discontinuities and their two-dimensional interactions. The motivation for this highorder methodology is to be able to capture shocks, and also have a high-order convergence in the rest of the domain, which is achieved as demonstrated in the current section. The simulation parameters used in the subsequent test cases are displayed in Table 1, where "VON" and "VOFF" stand for viscous regularization being turned on and off, respectively, in the isentropic Euler vortex test case. All other test cases include viscous regularization by default, as seen from Table 1. CFL numbers required to run each test case as calculated from Equation (60) are also presented in Table 1. Since the CFL number depends on the resolution, the smallest and the largest values, corresponding to the finest and the coarsest resolution for each test case, are presented. It can be observed that the viscous regularization lowers the CFL value, as is visible from the comparison between the Euler vortex VON and VOFF cases, making it especially restrictive in the Riemann problem case 3.

3.1. Isentropic Euler vortex problem

This problem describes the advection of a vortex with a constant speed. It has an analytical solution, which makes it a common test case for evaluating the accuracy and long-term stability of numerical codes [60–62]. The analytical solution is expressed as

$$u(\mathbf{x},t) = u_{\infty} - \frac{b}{2\pi} (y - v_{\infty}t)e^{1 - ((x - u_{\infty}t)^2 + (y - v_{\infty}t)^2)},$$

$$v(\mathbf{x},t) = v_{\infty} + \frac{b}{2\pi} (x - u_{\infty}t)e^{1 - ((x - u_{\infty}t)^2 + (y - v_{\infty}t)^2)},$$

$$T(\mathbf{x},t) = 1 - \frac{(\gamma - 1)b^2}{16\gamma\pi^2} (x - u_{\infty}t)e^{2(1 - (x - u_{\infty}t)^2 + (y - v_{\infty}t)^2)},$$

$$\rho(\mathbf{x},t) = T(\mathbf{x},t)^{\frac{1}{\gamma-1}}.$$
(61)

The test problem is numerically solved in the current work on a periodic square domain $(x, y) \in [-5, 5]^2$. Fig. 1 shows the density contours at time t = 0 corresponding to the initial conditions for this test problem. Here, we set u_∞ and v_∞ to 1 and 0, respectively, leading to a result that the vortex only propagates in the x direction. One period, or one flow through time (FTT), in this configuration is t = 10. For the strength of the vortex, b is set to 5. Since there are no discontinuities in this case, the viscous regularization is originally turned off (VOFF case).

To test the accuracy, we compute the L^2 error at 1 FTT using both the h-refinement and the p-refinement. The L^2 error and the convergence rate are defined as follows,

$$\|\epsilon\|_{2} = \sqrt{\frac{\int_{\Omega} |\mathbf{U} - \mathbf{U}_{ext}|^{2} d\Omega}{\int_{\Omega} 1 d\Omega}},$$
(62)

$$rate_{i} = \frac{\log(\|\epsilon_{i-1}\|_{2} / \|\epsilon_{i}\|_{2})}{\log(h_{i-1}/h_{i})},$$
(63)

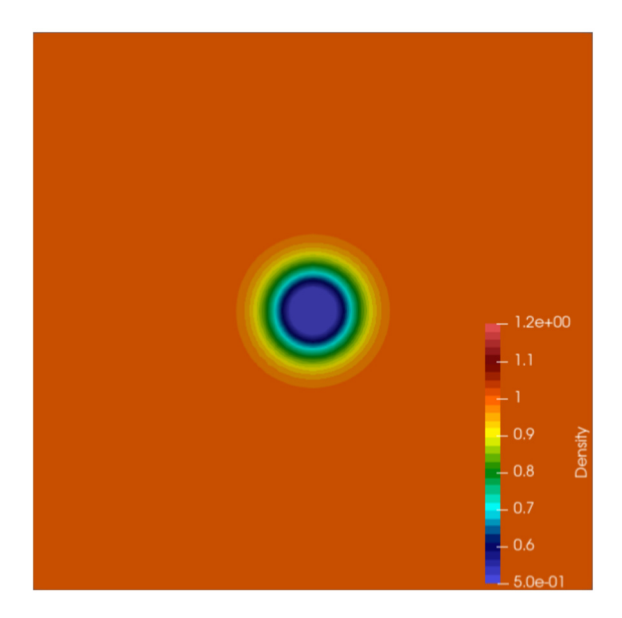


Fig. 1. Density contour of the initial condition for the isentropic Euler vortex problem.

Table 2 L^2 norm of errors of ρ in isentropic Euler vortex problem at t= 10 (1 FIT).

N=6			N = 8			N = 10		
h	L ² error	rate	h	L ² error	rate	h	L ² error	rate
10/20	1.21E-05	-	10/12	7.00E-06	-	10/12	3.35E-07	-
10/24	5.50E-06	4.30	10/16	9.53E-07	6.93	10/16	2.10E-08	9.63
10/30	1.41E-06	6.04	10/20	1.61E-07	7.98	10/20	2.56E-09	9.43
10/36	4.90E-07	5.86	10/24	3.71E-08	8.05	10/24	3.31E-10	11.23

Table 3 L^2 norm of errors of ρu in isentropic Euler vortex problem at t = 10 (1 FIT).

N = 6			N = 8			N = 10		
h	L ² error	rate	h	L ² error	rate	h	L ² error	rate
10/20	9.39E-06	-	10/12	7.49E-06	-	10/12	4.21E-07	-
10/24	8.71E-06	0.41	10/16	1.25E-06	6.22	10/16	2.34E-08	10.04
10/30	1.28E-06	8.60	10/20	1.96E-07	8.32	10/20	2.71E-09	9.66
10/36	3.68E-07	6.84	10/24	8.52E-08	4.56	10/24	4.50E-10	9.86

Table 4 L^2 norm of errors of ρv in isentropic Euler vortex problem at t=10 (1 FIT).

N=6			N = 8			N = 10		
h	L ² error	rate	h	L ² error	rate	h	L ² error	rate
10/20	8.85E-06	-	10/12	5.63E-06	-	10/12	3.15E-07	-
10/24	4.31E-06	3.94	10/16	6.31E-07	7.60	10/16	1.65E-08	10.25
10/30	1.01E-06	6.52	10/20	1.11E-07	7.80	10/20	1.78E-09	9.99
10/36	3.53E-07	5.75	10/24	3.26E-08	6.71	10/24	2.99E-10	9.78

where, the integral in Equation (62) is evaluated using the GLL quadrature law, in Equation (63), i = 2, 3, 4 correspond to the h-refinement levels form the baseline (coarsest) level of i = 1, \mathbf{U} is the solution vector for the numerical solution, and \mathbf{U}_{ext} is the solution vector for the exact solution. Details of the h-refinement study can be seen in Tables 2 to 5 for different polynomial orders. Here, N refers to the number of GLL points per element per direction, while the polynomial order of approximation is equal to N-1. Optimal convergence rates are obtained in different ranges of h for different polynomial orders. Under p-refinement, the element length h is set to 10/4, resulting in 16 uniform elements within the domain, which is coarser than the i=1 level of the h-refinement study. As expected, the error drops exponentially when we increase the polynomial order, demonstrated in Fig. 2. From Tables 2 to 5, we can also notice that higher-order cases are more accurate than the lower-order ones with the same or even fewer degrees of freedom (DOFs). Here, the number of DOFs is defined

Table 5 L^2 norm of errors of ρe in isentropic Euler vortex problem at t = 10 (1 FIT).

N = 6			N = 8			N = 10		
h	L ² error	rate	h	L ² error	rate	h	L ² error	rate
10/20	3.47E-05	-	10/12	1.64E-05	-	10/12	9.44E-07	-
10/24	1.50E-05	4.60	10/16	2.17E-06	7.03	10/16	4.63E-08	10.48
10/30	3.57E-05	6.44	10/20	3.81E-06	7.79	10/20	6.12E-09	9.06
10/36	1.38E-06	5.20	10/24	1.09E-07	6.84	10/24	1.04E-09	9.75

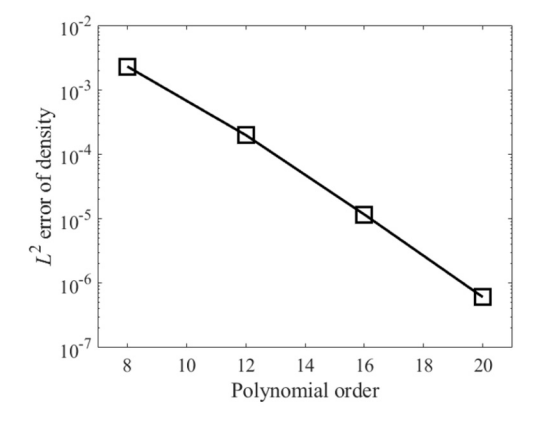


Fig. 2. L^2 error of density after 1 FTT for the isentropic Euler vortex problem.

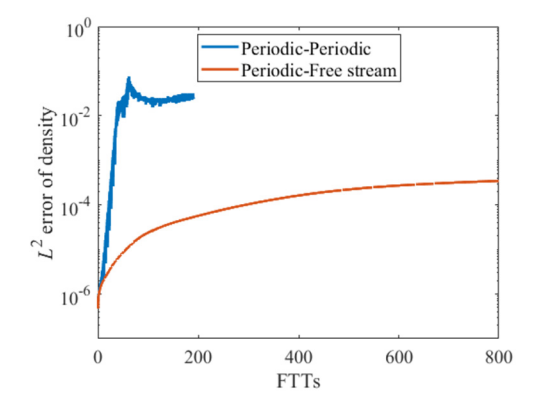
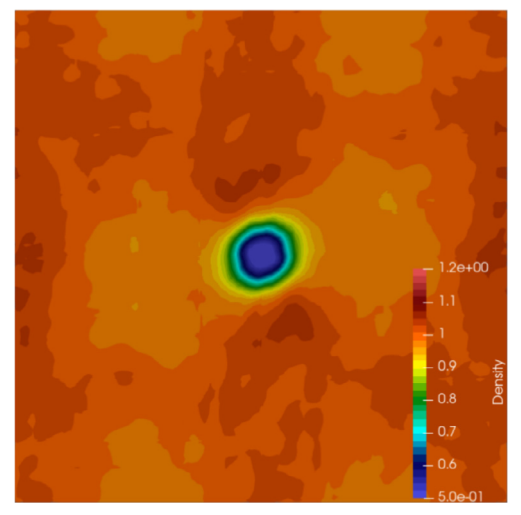


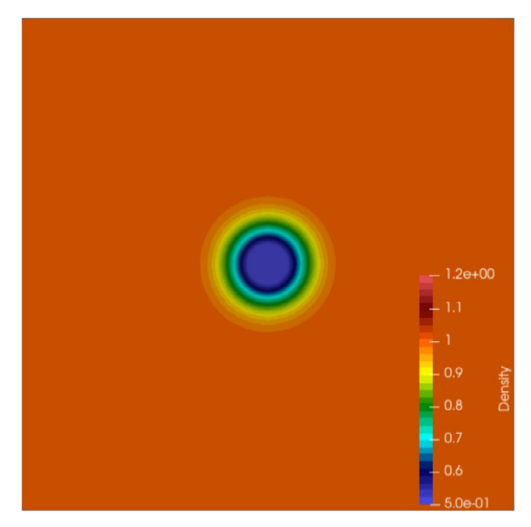
Fig. 3. L^2 error of density after long simulation time for the isentropic Euler vortex problem with h = 10/8 and N = 12.

as the total number of solution points. In Table 2, for example, the coarsest case of N = 10 (corresponding to a polynomial order of 9), with $(12 \times 10)^2 = 120^2$ DOFs, has a smaller L^2 error than the finest case of N = 6 which has 216^2 DOFs.

We subsequently look into long-term stability properties of the developed methodology using this problem. The domain is decomposed into 8×8 uniform square elements. Within each element, there are 12 GLL points in each direction. From the results in Fig. 3 we can see that if the periodic-periodic boundary condition is imposed, the error increases rapidly. By 139 periods, a significant contamination caused by the instability occurs in the domain (see Fig. 4). Similar issues related to long-term stability of the computations of the convecting compressible Euler vortex were also reported in [62]. Although the authors of [62] didn't comment on a potential cause of this instability, another study [61] mentioned that by changing the boundary conditions in a direction normal to the vortex propagation (on both sides of the domain) to a free-stream boundary condition, the distortion of the solution in a long-time computation can be diminished. Here, freestream boundary conditions correspond to a Dirichlet if a flow is entering the domain, and Neumann, if it is leaving the domain. When imposing periodic-free stream boundary conditions, robust long-term stability characteristics are achieved. The error keeps at least two orders of magnitude lower than in the periodic-periodic case after 130 periods and still remains considerably low even after 800 periods. Visually, there are no observable oscillations occurring in the density contour plot (Fig. 4(b)). This long-term stability property is further tested by simulations with different polynomial orders but the same number of DOFs (Fig. 5), such as N=4, N=8, in addition to already presented N=12 case. All the three cases are able to run stably until 800 FTTs. We again observe that with the same number of DOFs, the higher the polynomial order, the lower the error.



(a) PI flux with periodic boundary condition in y direction after 139 FTT



(b) PI flux with free-stream boundary condition in y direction after 800 FTT

Fig. 4. Density contours from different boundary conditions and simulation times. Periodic boundary conditions are used in *x* direction for all the cases. PI flux with free-stream boundary conditions in *y* direction was the case that was able to run until 800 FTT.

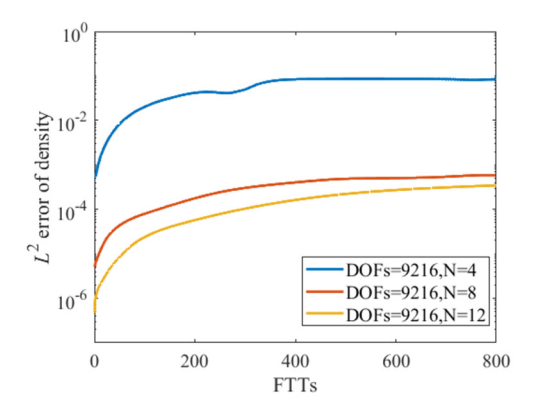


Fig. 5. L^2 error of density for up to 800 FTTs with different polynomial orders.

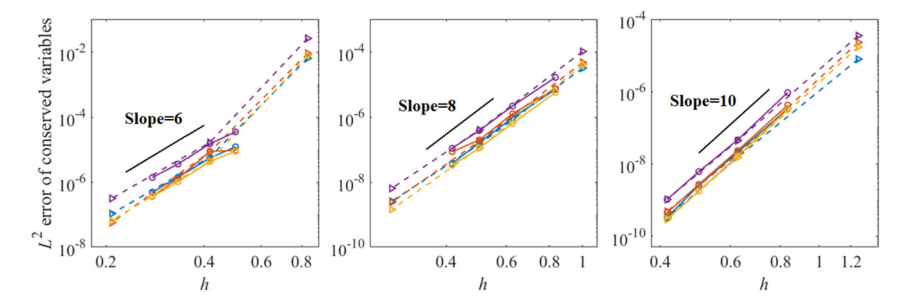


Fig. 6. L^2 error of conserved variables at t=1 FTT for isentropic Euler vortex problem with different polynomial orders, N=6 (left), N=8 (mid) and N=10 (right). In each sub-figure, we compare the L^2 error using the two settings with the viscous regularization off (circles) and on (triangles) for ρ (blue), ρu (red), ρv (yellow) and ρE (violet). Black solid line represents the optimal order of convergence for different polynomial orders and free-stream boundary conditions.

The above results are all obtained with the viscous regularization turned off. In order to study the effect of the viscous regularization on the smooth solutions, we now compare this with the case where the viscous regularization is turned on with $\{c^*, c_{max}, \mathcal{P}, \beta\} = \{10, 0.5, 0.7, 0.01\}$, the same set of parameter values used in all the other test cases. We also set $\alpha = 1$ to include the effect of the penalty term in Equation (54). The comparison is shown in Fig. 6. The errors agree well, so we can conclude that the viscous regularization doesn't affect the accuracy in the smooth area, which is expected.

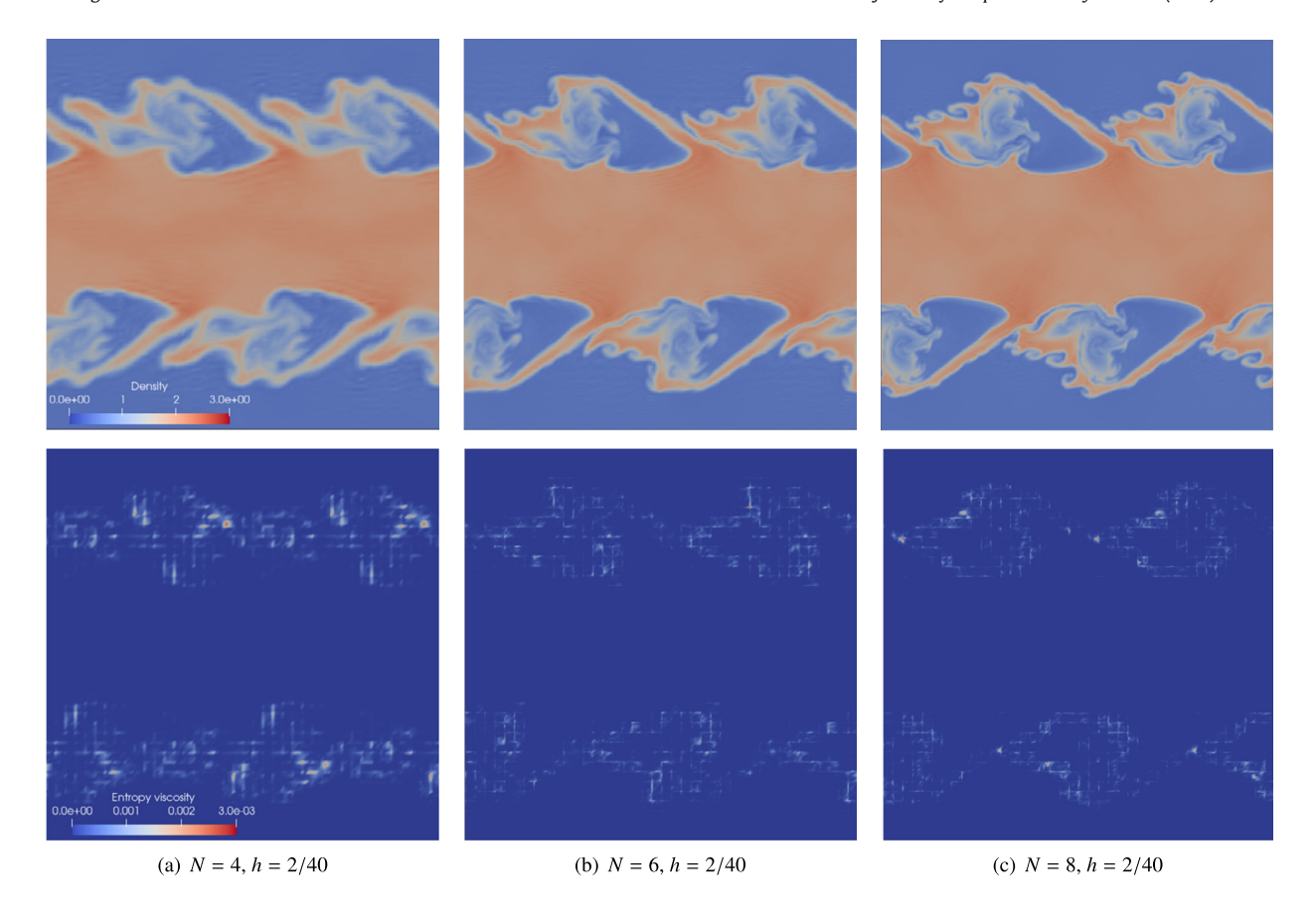


Fig. 7. Density (top) and entropy viscosity coefficient (bottom) contours for the Kelvin-Helmholtz instability problem with different polynomial orders at t = 3.7. Each snapshot corresponds to a whole domain $[-1, 1]^2$.

3.2. 2D Kelvin-Helmholtz instability

The inviscid Kelvin-Helmholtz instability test case is initialized on a periodic domain $[-1, 1]^2$ in a subsonic, shock-free manner, with

$$p = 1,$$

$$\rho = \frac{1}{2} + \frac{3}{4}B,$$

$$u = \frac{1}{2}(B - 1),$$

$$v = \frac{1}{10}\sin(2\pi x),$$
(64)

where $B = \tanh(15y + 7.5) - \tanh(15y - 7.5)$ [34]. The simulation quickly gets under-resolved due to the development of the shear layers with the absence of viscosity. It turns out that with the split-form DGSEM alone, the simulation is not stable and will blow up in a relatively short time, under t = 5. With the help of the viscous regularization, all the three simulations with different polynomial orders (h = 2/40 and N = 4, 6 and 8) can run without stability issues past t = 20. At t = 3.7, our results in Fig. 7 show similar patterns with the ones in [34]. Apparently, our result with N = 4 is more dissipative, which is due to the fewer DOFs used compared to the results in [34]. When N increases to 6, the total number of DOFs is close to the one used in [34], thus the results are comparable. We can see from the entropy viscosity coefficient contours shown in Fig. 7 that the viscous regularization is activated locally at each GLL point, rather than attaining a uniform value across the elements. It retains the accuracy of the "smoother" area as much as possible. As the structures develop to t = 20 (see Fig. 8), completely different patterns are observed. This is the result of the strong non-linearity of this test case.

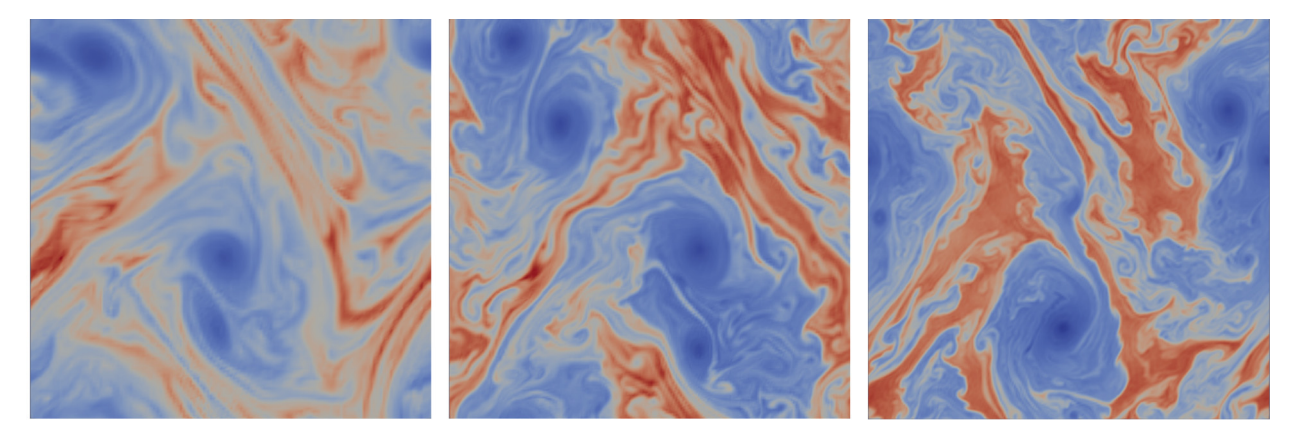


Fig. 8. Density contours, from 0.4 to 2.4 with 256 levels, for the Kelvin-Helmholtz instability problem with h = 2/40 and N = 4 (left), N = 6 (mid), N = 8 (right) at t = 20. Each snapshot corresponds to a whole domain $[-1, 1]^2$.

Table 6 L^1 error of density in Sod shocktube case.

N=4			N = 6			N = 8		
DOFs	L ¹ error	rate	DOFs	L ¹ error	rate	DOFs	L ¹ error	rate
100	1.32E-02	-	150	8.00E-03	-	200	5.50E-03	-
200	6.94E-03	0.9295	300	4.18E-03	0.9376	400	3.01E-03	0.8706
400	3.47E-03	1.0022	600	2.20E-03	0.9216	800	1.66E-03	0.8576

Table 7 L^2 error of density in Sod shocktube case.

N=4			N = 6	N = 6			N = 8		
DOFs	L ² error	rate	DOFs	L ² error	rate	DOFs	L ² error	rate	
100	2.25E-02	-	150	1.62E-02	-	200	1.17E-02	-	
200	1.40E-02	0.6905	300	9.51E-03	0.7595	400	7.50E-03	0.6442	
400	8.44E-03	0.7263	600	6.17E-03	0.6244	800	5.39E-03	0.4767	

3.3. Sod shocktube problem

Sod shocktube problem [54] is initialized as

$$(\rho, u, p) = \begin{cases} (1, 0, 1), x \le 0, \\ (0.125, 0, 0.1), x > 0, \end{cases}$$
 (65)

on the domain $x \in [-0.5, 0.5]$. All results are obtained at t = 0.2. The exact solution is calculated using the method of characteristics [54]. The h-refinement convergence study is done under the polynomial orders N = 4, 6, 8 (see Fig. 9). The results are converging to the exact solution as we refine the mesh. Results from the convergence study are displayed in Tables 6 through 8. The L^1 and L^2 error of density under different resolutions, and the corresponding convergence rates are calculated. The convergence rates of L^1 and L^2 errors are close to their theoretical values of 1 and 0.5, respectively, in the presence of discontinuities [63], in nearly all the cases, which is comparable to the results from other numerical tests [40,42]. We also notice that the p-refinement leads to a slight drop of the convergence rate, which is also observed in [40]. However, an opposite trend is documented in [42]. The reason behind this difference requires further investigation and might depend on the specific details of a numerical method. Further, we compare the absolute values of L^1 and L^2 errors between high-order cases and low-order cases. The errors for the same or equivalent number of degrees of freedom are directly compared in Table 8. It can be appreciated that the higher-order setup results in lower error at the same number of DOFs, both for L^1 and L^2 errors. We can further observe this trend in Fig. 10, where a higher order approximation shows a better agreement with the exact solution in the vicinity of discontinuities, but this advantage is not as obvious in the smooth areas.

3.4. Lax problem

The Lax problem is also a member of the shocktube test problems. Thus, like the Sod shocktube problem, the analytical solution is available for the convergence studies. This case is initialized as

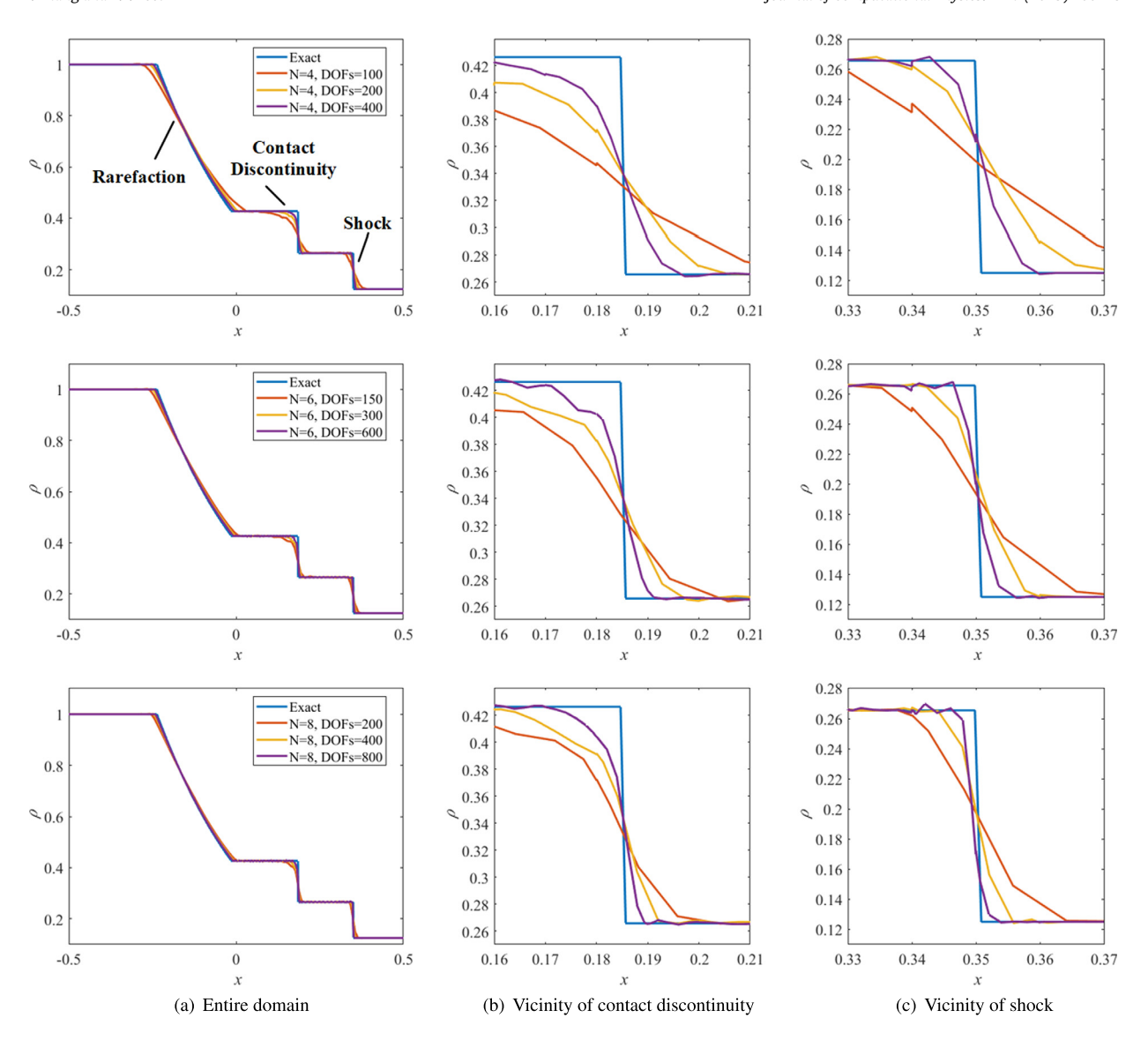


Fig. 9. Density distribution for the Sod shocktube problem with different polynomial orders and grid sizes at t = 0.2.

Table 8 L^1 and L^2 error of density in Sod shocktube case with the equivalent number of DOFs and different polynomial orders.

N=4			N = 6			N = 8		
DOFs	L ¹ error	L ² error	DOFs	L ¹ error	L ² error	DOFs	L ¹ error	L ² error
200 400	6.94E-03 3.47E-03	1.40E-02 8.44E-03	204 402	6.00E-03 3.06E-03	1.25E-02 8.39E-03	200 400	5.50E-03 3.01E-03	1.17E-02 7.50E-03

$$(\rho, u, p) = \begin{cases} (0.445, 0.698, 3.528), x \le 0, \\ (0.5, 0, 0.571), x > 0, \end{cases}$$
(66)

on the domain $x \in [-5, 5]$. All the results are obtained at t = 0.13, as presented in Figs. 11 and 12. The convergence rates of L^1 and L^2 errors are close to the theoretical values, 1 and 0.5, respectively, for most of the cases, as can be observed from Tables 9 and 10. We also conduct comparisons between the cases with the same number of DOFs but different polynomial orders. The previous conclusion that the cases with higher polynomial order have lower errors also holds for the Lax problem.

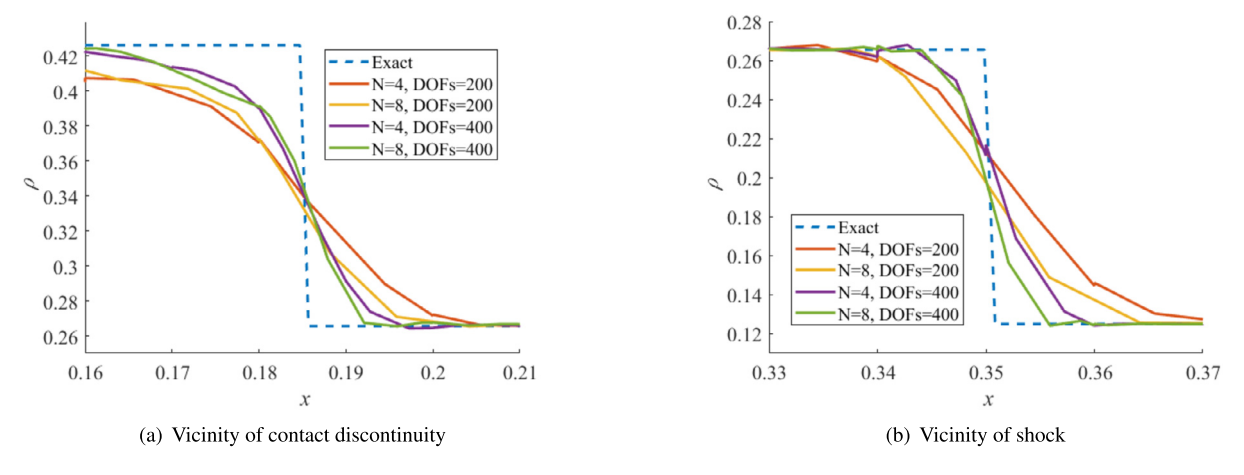


Fig. 10. Density distribution for the Sod shocktube problem using different refinement plans at t = 0.2.

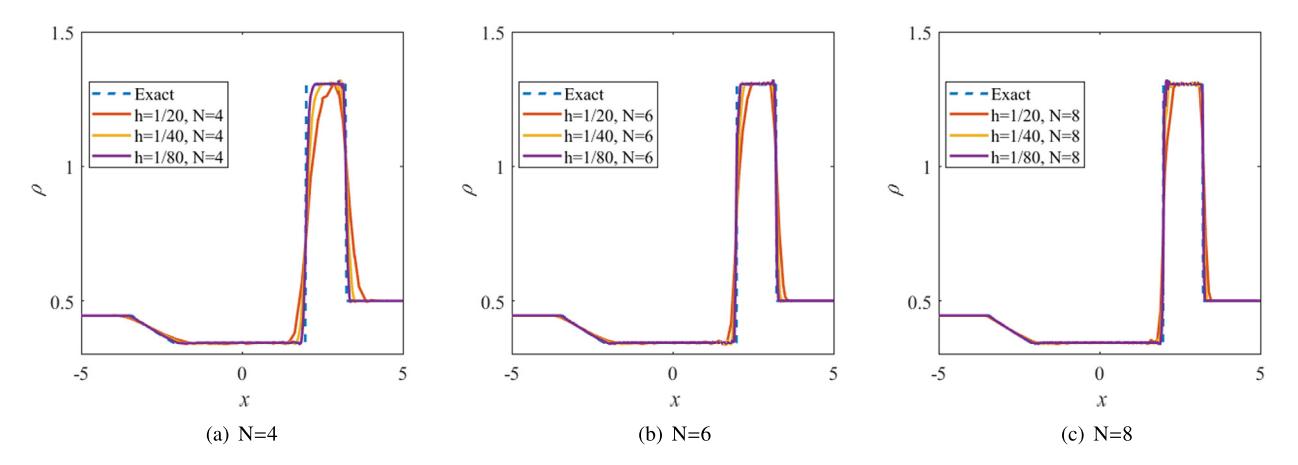


Fig. 11. Density distribution for the Lax problem under different polynomial orders and grid sizes at t = 0.13.

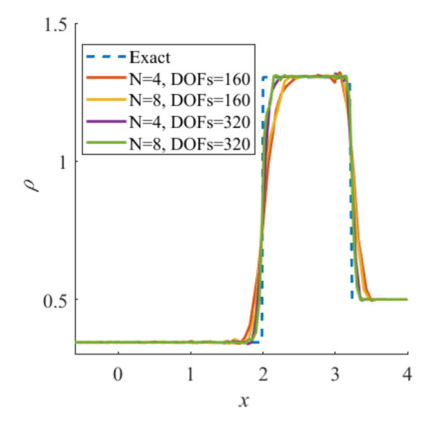


Fig. 12. Density distribution for the Lax problem around the density waves using different refinement plans at t = 0.13.

Table 9 L^1 error of density in Lax problem.

N = 4	N=4			N = 6			N = 8		
DOFs	L ¹ error	rate	DOFs	L ¹ error	rate	DOFs	L ¹ error	rate	
80 160	1.47E-02	- 0.9697	120 240	8.69E-03	- 0.9647	160 320	1.20E-02 5.96E-03	1.0074	
320	7.38E-03	0.9973	480	4.79E-03	0.8589	640	3.43E-03	0.7986	

Table 10 L^2 error of density in Lax problem.

N=4			N = 6			N = 8		
DOFs	L ² error	rate	DOFs	L ² error	rate	DOFs	L ² error	rate
80	8.69E-02	-	120	6.07E-02	-	160	4.96E-02	-
160	6.15E-02	0.4984	240	4.41E-02	0.4589	320	3.55E-02	0.4811
320	4.14E-02	0.5721	480	3.47E-02	0.3488	640	2.85E-02	0.3156

3.5. Shu-Osher problem

This test case models the interaction of a moving Mach 3 shock wave with high-frequency density waves [55]. The ability to capture small-scale structures in the near-shock region tested by this problem is crucial in many important cases, e.g., during shock wave/boundary layer interaction. The problem is initialized as

$$(\rho, u, p) = \begin{cases} (3.857143, 2.629369, 10.333333), x \le -3/8, \\ (1 + 0.2\sin(50x), 0, 1), x > -3/8, \end{cases}$$

$$(67)$$

on a domain $x \in [-0.5, 0.5]$. All data is collected at t = 0.18. Due to the absence of an analytical solution for this problem, the reference value is obtained using the same numerical method with 2000 elements and a polynomial order of 5. The density distributions obtained under different polynomial orders and grid sizes as compared to a reference solution are shown in Fig. 13. For the coarsest case, with h = 1/25 and N = 4 corresponding to 100 DOFs, the density waves are not resolved at all. After we conduct both p-refinement and h-refinement to reach 600 DOFs, the structure is well-resolved. Similarly to what we found in the shocktube case, the p-refinement is also more efficient in this case. This is demonstrated in Fig. 14. We can get 200 and 400 DOFs by applying different refinement plans, e.g. 400 DOFs can be decomposed into 50 elements with a polynomial order of 7 (N = 8), or 100 elements with a polynomial order of 3 (N = 4). Fig. 14 confirms that higher-order refinement plans provide better performance, especially in the vicinity of troughs.

3.6. Mach 3 forward step problem

The Mach 3 forward step problem was originally introduced in [56] and re-examined in [57] to compare several difference schemes. This problem is chosen in the current study to test the performance of the developed methodology in 2D cases with discontinuities. The same domain as in [57] is used for the current simulations, which is $(x, y) \in [0, 0.6] \times [0, 1] \cup [0.6, 3] \times [0.2, 1]$. Symmetry boundary condition is applied to the upper and lower boundaries, including the step boundary. The left and right boundary conditions are set to a supersonic inflow and outflow, respectively. The top row of Fig. 15 shows the results of the baseline case (h = 1/40, N=4) at t = 3. All typical structures, such as a bow shock, Mach stem, contact discontinuity, and a reflecting shock, are well captured as compared to [57]. We can see that the entropy viscosity is only activated near the shocks and at the step corner, while it is viscosity-free in the vicinity of the contact discontinuities, which is expected (see Fig. 15). Both the h— and p-refinement cases are able to capture the Kelvin-Helmholtz instability along the slip line. However, the case with p-refinement resolves apparently more structures than the h-refinement case.

It was previously noted that a step corner singularity gives rise to an artificial entropy layer at the bottom wall that creates certain artificial structures in the numerical solution [2,42,57]. It is seen from the work of [2,42] that these artificial structures come in the form of a Mach stem at the bottom wall at lower polynomial orders, while they transition into sharp inclined shock-like structures at higher polynomial orders. The existence of these structures was noted in spite of rounding the corner in [42]. Consistent with the previous observations, we do not get a Mach stem, but rather a shock-resembling structure, which is created where the reflecting shock hits the step wall, moves upstream towards the corner as the time progresses, and merges with another weaker shock that is formed close to the corner, as indicated in Fig. 15. These artificial structures can potentially be removed by either a modification of the numerical scheme near the corner [57], or an aggressive mesh refinement around the corner [2]. In this paper, we have opted not to resolve to any extra measures for this test case, since removing the singularity by itself is not the focus of this investigation, and, as seen from Fig. 15, the artificial structure shows no apparent effect on the major physical structures, at least until the end of the simulation time of t = 3, as compared with the previous results [2,42,57].

3.7. 2D Riemann problem case 3

This 2D Riemann problem divides the domain into four equal parts, and uniform initial conditions are applied in each subdomain. Different initial conditions will develop into different structures [58,59]. The initial condition for case 3 is set on a 2D domain $(x, y) \in [0, 1]^2$ as follows,

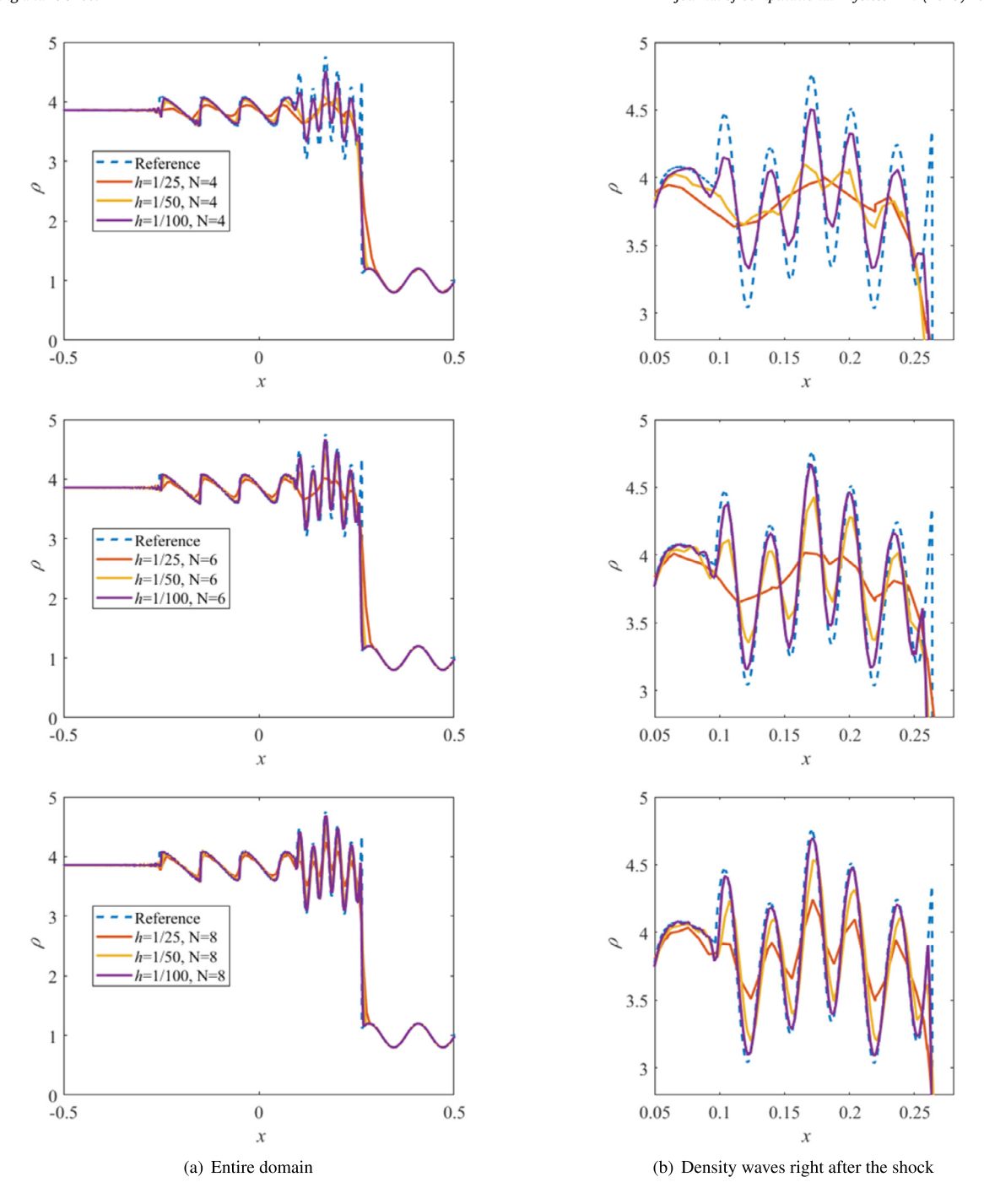


Fig. 13. Density distribution for the Shu-Osher problem under different polynomial orders and grid sizes at t = 0.18.

$$p = 0.3, \qquad \rho = 0.5323, \quad \mathbf{u} = (1.206, 0), \qquad \text{in} \quad 0 < x < 0.5, \quad 0.5 < y < 1,$$

$$p = 0.029, \quad \rho = 0.138, \quad \mathbf{u} = (1.206, 1.206), \quad \text{in} \quad 0 < x < 0.5, \quad 0 < y < 0.5,$$

$$p = 0.3, \quad \rho = 0.5323, \quad \mathbf{u} = (0, 1.206), \quad \text{in} \quad 0.5 < x < 1, \quad 0 < y < 0.5,$$

$$p = 1.5, \quad \rho = 1.5, \quad \mathbf{u} = (0, 0), \quad \text{in} \quad 0.5 < x < 1, \quad 0.5 < y < 1.$$

The computational domain is decomposed into 100×100 elements. As mentioned before, a penalty term for the shock capturing scheme in Equation (54) needs to be included in order to run this case, see also Table 1. In a previous numerical investigation [64], Neumann boundary condition, or a so-called outflow boundary condition was imposed for all the four

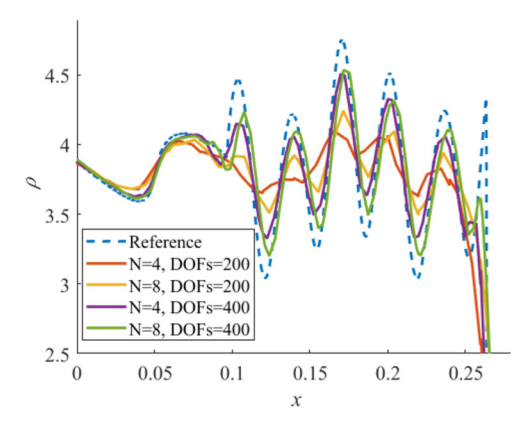


Fig. 14. Density distribution for the Shu-Osher problem around the density waves using different refinement plans at t = 0.18.

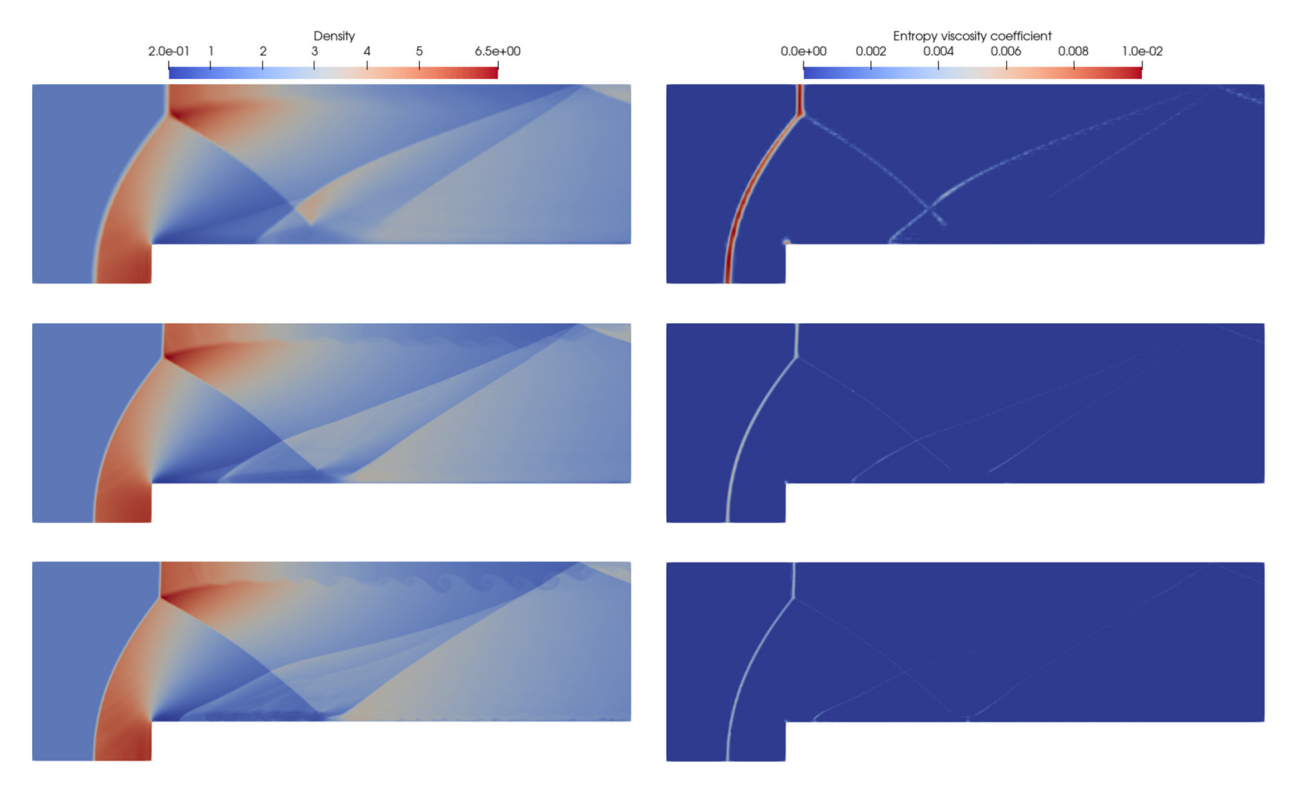


Fig. 15. Density (left) and entropy viscosity coefficient (right) contours for the forward step problem at t = 3 with different mesh refinement: baseline (top), h = 1/40, N = 4; h-refinement (mid), h = 1/80, N = 4; h-refinement (bottom), h = 1/40, N = 8.

boundaries. However, in our experience, this boundary condition doesn't work well in this case. Strong numerical oscillations are created at the discontinuities near the boundaries. Eventually the noise results in a divergence. Here, we impose a time-varying Dirichlet boundary condition to make the computation stable. Within a limited computation time, the boundaries can be considered as one-dimensional shocktube cases, whose analytical solutions are available. By initializing the case with the set of values as given in (68), the solution displays four shocks created on the boundaries of each of the two adjacent zones [58,59], which is represented correctly by the current numerical solution. Indeed, in Fig. 16, we see discontinuities at the interior edges in the density contours that are consistent with the initial conditions. Comparing our results to the results from previous literature [58,59,64,65], we can see that our solver accurately captures the core structures in the main region. With the *p*-refinement, more details, especially the structures related to the shear instability, are resolved as expected.

3.8. 2D Riemann problem case 15

The setup of this case is basically the same as the 2D Riemann problem case 3 described in Section 3.7, except for the initial condition, which now reads

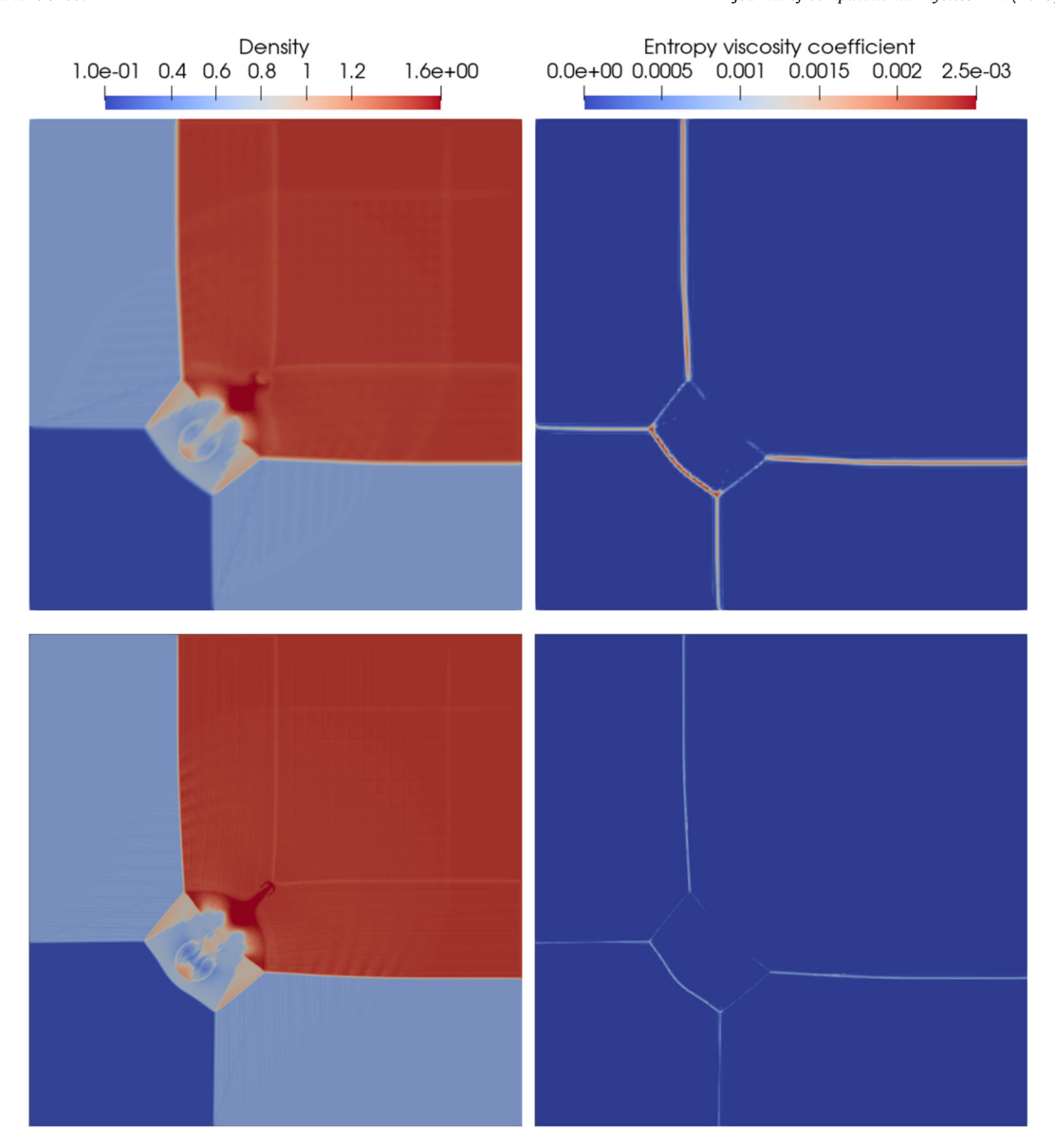


Fig. 16. Density (left) and entropy viscosity coefficient (right) contours for the 2D Riemann problem case 3 with different polynomial orders, top: h = 1/100, N = 4; bottom: h = 1/100, N = 8, at t = 0.3.

$$p = 0.4, \quad \rho = 0.5197, \quad \mathbf{u} = (-0.6259, -0.3), \quad \text{in} \quad 0 < x < 0.5, \quad 0.5 < y < 1,$$

$$p = 0.4, \quad \rho = 0.8, \quad \mathbf{u} = (0.1, -0.3), \quad \text{in} \quad 0 < x < 0.5, \quad 0 < y < 0.5,$$

$$p = 0.4, \quad \rho = 0.5313, \quad \mathbf{u} = (0.1, 0.4276), \quad \text{in} \quad 0.5 < x < 1, \quad 0 < y < 0.5,$$

$$p = 1, \quad \rho = 1, \quad \rho = 1, \quad \mathbf{u} = (0.1, -0.3), \quad \text{in} \quad 0.5 < x < 1, \quad 0.5 < y < 1.$$

For the boundary condition, we specify a locally one-dimensional solution of the Riemann problem developed out of the conditions (69), similarly to the setup in Section 3.7. With this set of initial conditions, the discontinuities near the boundaries are, counter-clockwise starting from the upper boundary, a rarefaction wave, a contact discontinuity, a contact discontinuity, and a shock [58,59]. In Fig. 17, the pattern developed in the center area agrees well with the other published work [58,59,64,65]. Kelvin-Helmholtz instability is observed along the density discontinuities in the higher-order case due to a higher resolution capability, as expected. While the entropy viscosity is only activated along the main shock in the N=8 case, in the lower order case, it is activated in the core area, along the weak shock in the center, and also near the contact discontinuities. As time progresses to t=0.3, more small-scale structures are captured along the contact discontinuities and in the core area (Fig. 18).

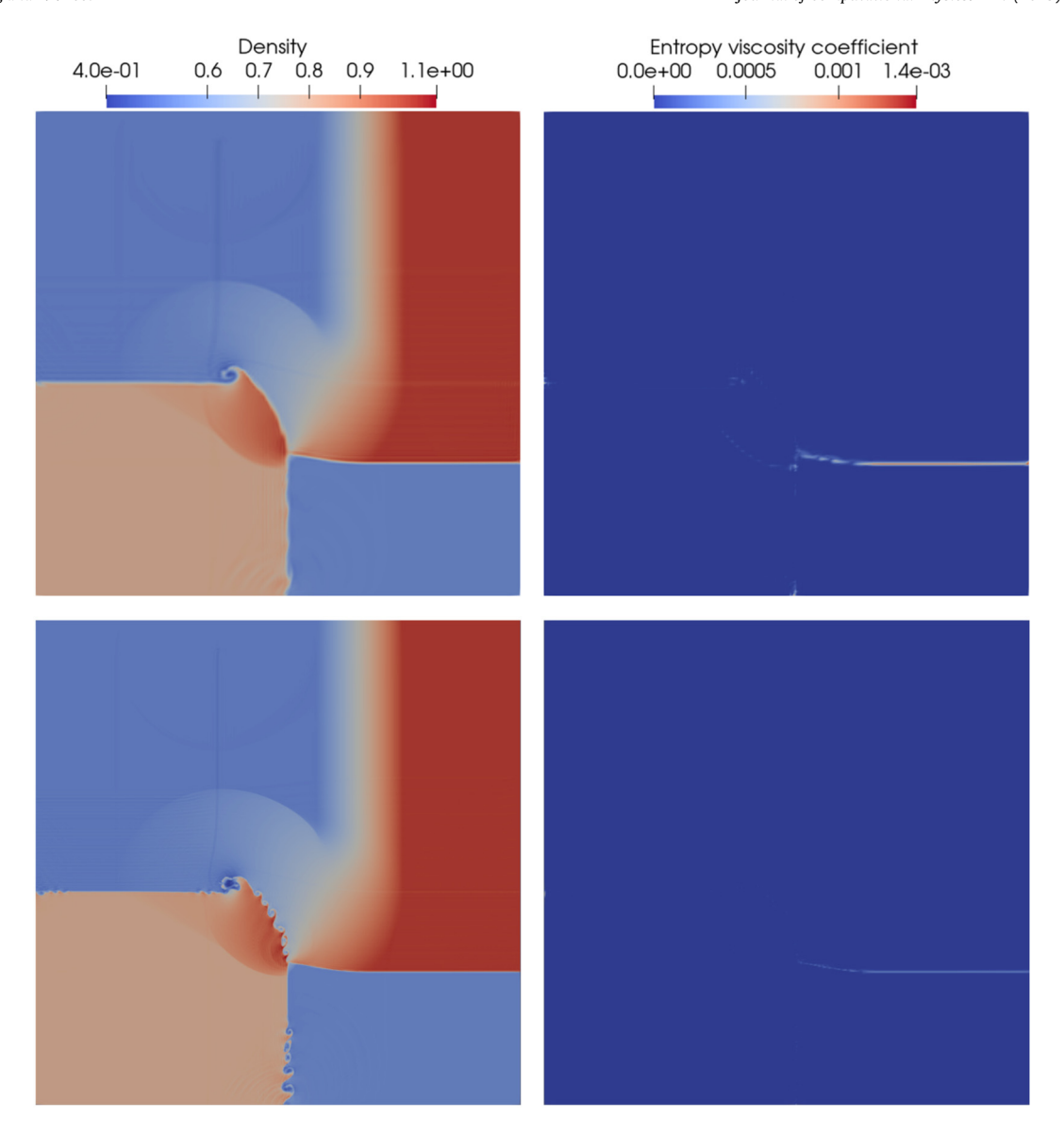


Fig. 17. Density (left) and entropy viscosity coefficient (right) contours for the 2D Riemann problem case 15 with different polynomial orders, top: h = 1/100, N = 4; bottom: h = 1/100, N = 8, at t = 0.2.

4. Conclusions

A high-order framework that uses discontinuous Galerkin spectral-element method to solve compressible Euler equations was developed. The summation by parts operator was introduced to the discrete approximation of the volume fluxes. Combining the SBP operator with the telescopic volume differencing relation and a two-point Pirozzoli flux formula, a kinetic energy preserving numerical scheme was obtained, which results in a provably stable formulation reducing an aliasing error [7,66]. To extend this split-form DGSEM formulation to the cases with discontinuities, a viscous regularization was introduced to the developed numerical methodology to enable shock capturing. The viscous regularization was only activated in the areas with sharp gradients, and the viscosity switch was controlled by an entropy-residual based shock detector combined with a Ducros sensor. While viscous regularization is an established framework for stabilization of compressible equations with shocks [3,37,42], to the authors' knowledge, its application within the split-form DGSEM methodology is new. In fact, split-form DGSEM methods were previously applied mostly with an element-wise subcell finite volume method for shock capturing. The current work serves as a useful exploration of split-form DGSEM methods with a gridpoint-wise shock capturing method enabled by an entropy viscosity formulation in the realm of discontinuous flow cases.

Two smooth and six discontinuous test cases were performed with the developed numerical methodology. For the 2D isentropic Euler vortex case, a high-order accuracy and a long-term stability were achieved using Pirozzoli flux augmented by a local Lax-Friedrichs dissipation term to estimate the interface flux. The results of Kelvin-Helmholtz problem showed

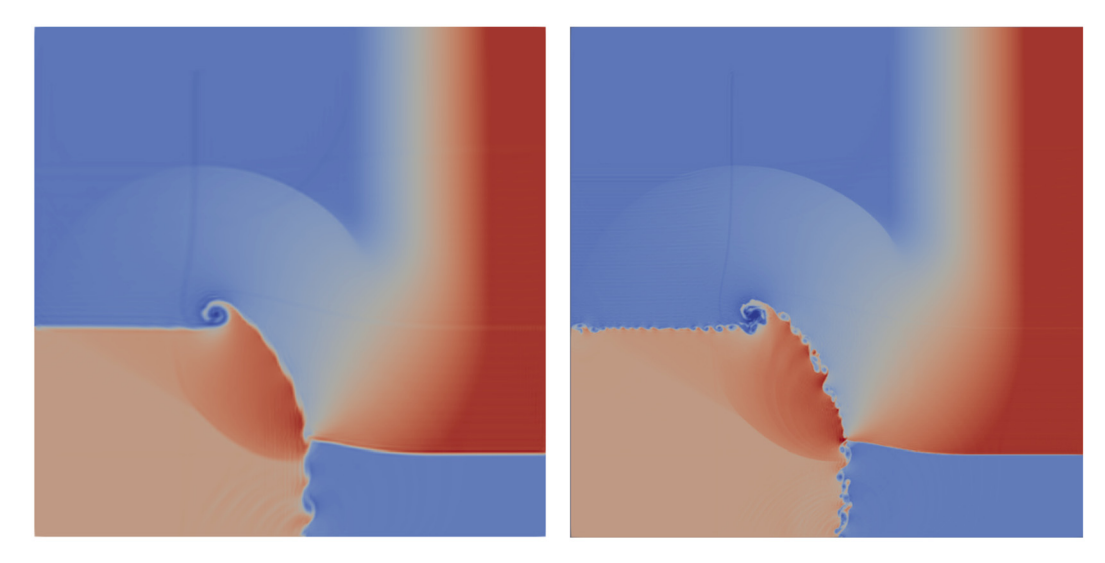


Fig. 18. Density contours for the 2D Riemann problem case 15 with different polynomial orders, left: h = 1/100, N = 4; right: h = 1/100, N = 8, at t = 0.3.

that even continuous cases, when under-resolved, may need additional techniques beyond the split-form DGSEM to stabilize the computations, and the proposed modified entropy viscosity method was able to achieve this with a little amount of added dissipation to retain the accuracy. From all the test cases with convergence studies, we found that the p-refinement was more efficient than the h-refinement. Indeed, p-refinement cases provided lower errors for the same number of degrees of freedom, which was the major motivation to pursue high-order methods. The developed methodology also demonstrated a good performance in 2D shocked problems. The method yielded an accurate representation of the physical structures formed due to the flow discontinuities in all the test cases. The resolution of a Kelvin-Helmholtz instability along the contact discontinuities in shocked cases indicates the high-order discretization capabilities of the solver in the presence of shocks. We also remark that the set of artificial viscosity parameter values, $\{c^*, c_{max}, \mathcal{P}, \beta\} = \{10, 0.5, 0.7, 0.01\}$, was considerably robust and was applied to all of the above test cases, while for the 2D Riemann problem case 3, an additional penalty term when discretizing the viscous fluxes in a shock capturing scheme was needed to ensure stability. Cases containing even stronger shocks, such as blast wave problems, may require additional stabilization techniques beyond what was presented in this paper, which is the subject of the future work. One possible drawback of the developed methodology is a restrictive time stability constraint in an explicit formulation due to an added dissipation as a result of the viscous shock capturing.

CRediT authorship contribution statement

Fengrui Zhang: Conceptualization, Methodology, Software, Validation, Visualization, Writing – original draft. **Yulia T. Peet:** Conceptualization, Funding acquisition, Supervision, Writing – original draft.

Declaration of competing interest

The authors declare that they have no known competing financial interests or personal relationships that could have appeared to influence the work reported in this paper.

Acknowledgements

This work was supported by NSF CBET grant # 1707075.

References

- [1] G.J. Gassner, A.D. Beck, On the accuracy of high-order discretizations for underresolved turbulence simulations, Theor. Comput. Fluid Dyn. 27 (2013) 221–237.
- [2] B. Cockburn, C.W. Shu, The Runge-Kutta discontinuous Galerkin method for conservation laws V: multidimensional systems, J. Comput. Phys. 141 (1998) 199–224.
- [3] P.O. Persson, J. Peraire, Sub-cell shock capturing for discontinuous Galerkin methods, in: AIAA 2006-112, 2006.
- [4] X. Zhong, C.W. Shu, A simple weighted essentially nonoscillatory limiter for Runge-Kutta discontinuous Galerkin methods, J. Comput. Phys. 232 (2013)
- [5] V. Zingan, J.L. Guermond, J. Morel, B. Popov, Implementation of the entropy viscosity method with the discontinuous Galerkin method, Comput. Methods Appl. Mech. Eng. 253 (2013) 479–490.
- [6] M.H. Carpenter, T.C. Fisher, E.J. Nielsen, S.H. Frankel, Entropy stable spectral collocation schemes for the Navier-Stokes equations: discontinuous interfaces, SIAM J. Sci. Comput. 36 (5) (2014) B835–B867.

- [7] G.J. Gassner, A.R. Winters, D.A. Kopriva, Split form nodal discontinuous Galerkin schemes with summation-by-parts property for the compressible Euler equations, J. Comput. Phys. 327 (2016) 39–66.
- [8] M. Bohm, S. Schermeng, A.R. Winters, G.J. Gassner, G.B. Jacobs, Multi-element SIAC filter for shock capturing applied to high-order discontinuous Galerkin spectral element methods, J. Sci. Comput. 81 (2019) 820–844.
- [9] D.A. Kopriva, Implementing Spectral Methods for Partial Differential Equations: Algorithms for Scientists and Engineers, 1st edition, Springer Publishing Company, Incorporated, 2009.
- [10] H.-O. Kreiss, G. Scherer, Finite element and finite difference methods for hyperbolic partial differential equations, in: Mathematical Aspects of Finite Elements in Partial Differential Equations, Academic Press, New York, 1974.
- [11] P. Olsson, Summation by parts, projections, and stability, Math. Comput. 64 (1995) 1035-1065.
- [12] M.H. Carpenter, J. Nordström, D. Gottlieb, A stable and conservative interface treatment of arbitrary spatial accuracy, J. Comput. Phys. 148 (1999) 341–365.
- [13] K. Mattsson, J. Nordström, Summation by parts operators for finite difference approximations of second derivatives, J. Comput. Phys. 199 (2004) 503–540.
- [14] G.J. Gassner, A skew-symmetric discontinuous Galerkin spectral element discretization and its relation to SBP-SAT finite difference methods, SIAM J. Sci. Comput. 35 (2013) A1233–A1253.
- [15] D.A. Kopriva, D.G. Gassner, An energy stable discontinuous Galerkin spectral element discretization for variable coefficient advection problems, SIAM J. Sci. Comput. 36 (2014) A2076–A2099.
- [16] M.H. Carpenter, M. Parsani, E.J. Nielsen, T.C. Fisher, Towards an entropy stable spectral element framework for computational fluid dynamics, AIAA Paper 2016–1058, in: Special Session: NASA's Revolutionary Computational Aerosciences I, 2016.
- [17] A.R. Winters, R.C. Moura, G. Mengaldo, G.J. Gassner, S. Walch, J. Peiro, S.J. Sherwin, A comparative study on polynomial dealiasing and split form discontinuous Galerkin schemes for under-resolved turbulence computations, J. Comput. Phys. 372 (2018) 1–21.
- [18] D.C. Del Rey Fernández, P.D. Boom, D.W. Zingg, A generalized framework for nodal first derivative summation-by-parts operators, J. Comput. Phys. 266 (2014) 214–239.
- [19] S. Ortleb, A kinetic energy preserving DG scheme based on Gauss-Legendre points, J. Sci. Comput. 71 (2017) 1135–1168.
- [20] G. Gassner, D.A. Kopriva, A comparison of the dispersion and dissipation errors of Gauss and Gauss-Lobatto discontinuous Galerkin spectral element methods, SIAM J. Sci. Comput. 33 (5) (2011) 2560–2579.
- [21] S.A. Orszag, On the elimination of aliasing in finite-difference schemes by filtering high-wavenumber components, J. Atmos. Sci. 28 (1971) 1074.
- [22] G. Patterson, S. Orszag, Spectral calculations of isotropic turbulence: efficient removal of aliasing interactions, Phys. Fluids 14 (1971) 2538–2541.
- [23] C. Canuto, M.Y. Hussaini, A. Quarteroni, T.A. Zang, Spectral Methods in Fluid Dynamics, Springer-Verlag, 1998.
- [24] R.M. Kirby, G.E. Karniadakis, De-aliasing on non-uniform grids: algorithms and applications, J. Comput. Phys. 191 (2003) 249-264.
- [25] P. Fischer, J. Mullen, Filter-based stabilization of spectral element methods, C. R. Acad. Sci., Ser. 1 Math. 332 (2001) 265-270.
- [26] J. Hesthaven, T. Warburton, Nodal Discontinuous Galerkin Methods: Algorithms, Analysis and Applications, Springer Verlag, New York, 2008.
- [27] C.A. Kennedy, A. Gruber, Reduced aliasing formulations of the convective terms within the Navier-Stokes equations for a compressible fluid, J. Comput. Phys. 227 (2008) 1676–1700.
- [28] S. Pirozzoli, Generalized conservative approximations of split convective derivative operators, J. Comput. Phys. 229 (2010) 7180-7190.
- [29] F. Ducros, F. Laporte, T. Soulères, V. Guinot, P. Moinat, B. Caruelle, High-order fluxes for conservative skew-symmetric-like schemes in structured meshes: application to compressible flows, J. Comput. Phys. 161 (2000) 114–139.
- [30] Y. Morinishi, Skew-symmetric form of convective terms and fully conservative finite difference schemes for variable density low-Mach number flows, J. Comput. Phys. 229 (2) (2010) 276–300.
- [31] T.C. Fisher, M.H. Carpenter, J. Nordström, N. Yamaleev, C. Swanson, Discretely conservative finite-difference formulations for nonlinear conservation laws in split form: theory and boundary conditions, J. Comput. Phys. 234 (1) (2013) 353–375.
- [32] N. Krais, A. Beck, T. Bolemann, H. Frank, D. Flad, G. Gassner, F. Hindenlang, M. Hoffmann, T. Kuhn, M. Sonntag, C. Munz, Flexi: a high order discontinuous Galerkin framework for hyperbolic-parabolic conservation laws, https://arxiv.org/pdf/1910.02858.pdf, 2019.
- [33] S. Hennemann, A.M. Rueda-Ramírez, F.J. Hindenlang, G.J. Gassner, A provably entropy stable subcell shock capturing approach for high order split form DG for the compressible Euler equations, J. Comput. Phys. 426 (2021) 109935.
- [34] A.M. Rueda-Ramírez, G.J. Gassner, A subcell finite volume positivity-preserving limiter for DGSEM discretizations of the Euler equations, in: WCCMEC-COMAS2020, 2021
- [35] J.X. Qiu, C.W. Shu, Runge-Kutta discontinuous Galerkin method using WENO limiters, SIAM J. Sci. Comput. 26 (2005) 907-929.
- [36] J. Zhu, J.X. Qiu, C.W. Shu, M. Dumbser, Runge-Kutta discontinuous Galerkin method using WENO limiters II: unstructured meshes, J. Comput. Phys. 227 (2008) 4330–4353.
- [37] J.L. Guermond, R. Pasquetti, B. Popov, Entropy viscosity method for nonlinear conservation laws, J. Comput. Phys. 230 (11) (2011) 4248-4267.
- [38] H. Abbassi, F. Mashayek, G.B. Jacobs, Shock capturing with entropy-based artificial viscosity for staggered grid discontinuous spectral element method, Comput. Fluids 98 (2014) 152–163.
- [39] M.O. Delchini, J.C. Ragusa, R.A. Berry, Entropy-based viscous regularization for the multi-dimensional Euler equations in low-Mach and transonic flows, Comput. Fluids 118 (2015) 225–244.
- [40] J.L. Guermond, B. Popov, V. Tomov, Entropy-viscosity method for the single material Euler equations in Lagrangian frame, Comput. Methods Appl. Mech. Eng. 300 (2016) 402–426.
- [41] Y. Lv, Y.C. See, M. Ihme, An entropy-residual shock detector for solving conservation laws using high-order discontinuous Galerkin methods, J. Comput. Phys. 322 (2016) 448–472.
- [42] M. Nazarov, A. Larcher, Numerical investigation of a viscous regularization of the Euler equations by entropy viscosity, Comput. Methods Appl. Mech. Eng. 317 (2017) 128–152.
- [43] T. Hendrickson, A. Kartha, G.V. Candler, An improved Ducros sensor for the simulation of compressible flows with shocks, in: AIAA 2018-3710, 2018.
- [44] P. Fischer, J. Lottes, S. Kerkemeier, O. Marin, K. Heisey, A. Obabko, E. Merzari, Y. Peet, Nek5000 user's manual, Technical Report ANL/MCS-TM-351, Argonne National Laboratory, http://nek5000.mcs.anl.gov, 2015.
- [45] E.F. Toro, Riemann Solvers and Numerical Methods for Fluid Dynamics, 1st edition, Springer Verlag, Berlin, 1999.
- [46] P.D. Lax, Weak solutions of nonlinear hyperbolic equations and their numerical approximation, Commun. Pure Appl. Math. 7 (1954) 159-193.
- [47] R.C. Moura, G. Mengaldo, J. Peiro, S.J. Sherwin, On the Eddy-resolving capability of high-order discontinuous Galerkin approaches to implicit LES / under-resolved DNS of Euler turbulence, J. Comput. Phys. 330 (2017) 615–623.
- [48] T.C. Fisher, M.H. Carpenter, High-order entropy stable finite difference schemes for nonlinear conservation laws: finite domains, J. Comput. Phys. 252 (2013) 518–557.
- [49] F. Ismail, P.L. Roe, Affordable, entropy-consistent Euler flux functions II: entropy production at shocks, J. Comput. Phys. 228 (2009) 5410-5436.
- [50] P. Chandrashekar, Kinetic energy preserving and entropy stable finite volume schemes for compressible Euler and Navier-Stokes equations, Commun. Comput. Phys. 14 (2013) 1252–1286.
- [51] F. Bassi, S. Rebay, A high-order accurate discontinuous finite element method for the numerical solution of the compressible Navier-Stokes equations, J. Comput. Phys. 131 (1997) 267–279.

- [52] M. Alhawwary, Z. Wang, A combined-mode Fourier analysis of DG methods for linear parabolic problems, SIAM J. Sci. Comput. 42 (6) (2020) A3825–A3858.
- [53] S. Gottlieb, C.W. Shu, Total variation diminishing Runge-Kutta schemes, Math. Comput. 67 (1998) 73-85.
- [54] G. Sod, A survey of several finite difference methods for systems of nonlinear hyperbolic conservation laws, J. Comput. Phys. 27 (1978) 606-614.
- [55] C.W. Shu, S. Osher, Efficient implementation of essentially non-oscillatory shock-capturing schemes II, J. Comput. Phys. 83 (1989) 32-78.
- [56] A.F. Emery, An evaluation of several differencing methods for inviscid fluid flow problems, J. Comput. Phys. 2 (1968) 306-331.
- [57] P. Woodward, P. Colella, The numerical simulation of two-dimensional fluid flow with strong shocks, J. Comput. Phys. 54 (1984) 115-173.
- [58] C.W. Schulz-Rinne, J.P. Collins, H.M. Glaz, Numerical solution of the Riemann problem for two-dimensional gas dynamics, SIAM J. Sci. Comput. 14 (1993) 1394–1414.
- [59] P.D. Lax, X.D. Liu, Solution of two-dimensional Riemann problems of gas dynamics by positive schemes, SIAM J. Sci. Comput. 19 (2) (1998) 319-340.
- [60] C.W. Shu, Essentially non-oscillatory and weighted essentially non-oscillatory schemes for hyperbolic conservation laws, in: A. Quarteroni (Ed.), Advanced Numerical Approximation of Nonlinear Hyperbolic Equations, in: Lecture Notes in Mathematics, vol. 1697, Springer, Berlin, Heidelberg, 1998.
- [61] P. Vincent, P. Castonguay, A. Jameson, Insights from von Neumann analysis of high-order flux reconstruction schemes, J. Comput. Phys. 230 (2011) 8134–8154.
- [62] S.C. Spiegel, H.T. Huynh, J.R. Debonis, A survey of the isentropic Euler vortex problem using high-order methods, AIAA Paper 2015-2444, in: 22nd AIAA Computational Fluid Dynamics Conference, Dallas, TX, 2015.
- [63] R.A. DeVore, Nonlinear approximation, Acta Numer. 7 (1998) 51-150.
- [64] R. Liska, B. Wendroff, Comparison of several difference schemes on 1D and 2D test problems for the Euler equations, SIAM J. Sci. Comput. 25 (3) (2003) 995–1017.
- [65] A. Kurganov, E. Tadmor, Solution of two-dimensional Riemann problems for gas dynamics without Riemann problem solvers, Numer. Methods Partial Differ. Equ. 18 (2002) 584–608.
- [66] J. Manzanero, G. Rubio, E. Ferrer, E. Valero, D.A. Kopriva, Insights on aliasing driven instabilities for advection equations with application to Gauss-Lobatto discontinuous Galerkin methods, SIAM J. Sci. Comput. 75 (2018) 1262–1281.